Influence of intermetallic Al−Mn particles on in-situ steam Mg−Al−LDH coating on AZ31 magnesium alloy

Feng LI[1*], Xiang SUN[1*], Liang SONG[1], M. Bobby KANNAN[2,3], Fen ZHANG[1], Lan-yue CUI[1],
Yu-hong ZOU[4], Shuo-qi LI[1], Cheng-bao LIU[1], Rong-chang ZENG[1,5]

1. Corrosion Laboratory for Light Metals, College of Materials Science and Engineering,
Shandong University of Science and Technology, Qingdao 266590, China;
2. School of Engineering, University of Newcastle, Callaghan, New South Wales 2308, Australia;
3. College of Science and Engineering, James Cook University, Townsville, Queensland 4811, Australia;
4. College of Chemical and Environmental Engineering,
Shandong University of Science and Technology, Qingdao 266590, China;
5. School of Materials Science and Engineering, Zhengzhou University, Zhengzhou 450002, China

Abstract: The influence of intermetallic Al−Mn particles on the corrosion behavior of in-situ formed Mg−Al layered double hydroxide (Mg−Al−CO_3^{2-}−LDH) steam coating on AZ31 Mg alloy was investigated. The alloy was pretreated with H_3PO_4, HCl, HNO_3 or citric acid (CA), followed by hydrothermal treatment, for the fabrication of Mg−Al−LDH coating. The microstructure, composition and corrosion resistance of the coated samples were investigated. The results showed that the surface area fraction of Al−Mn phase exposed on the surface of the alloy was significantly increased after CA pretreatment, which promotes the growth of the Mg−Al−LDH steam coating. Further, the LDH-coated alloy pretreated with CA possessed the most compact surface and the maximum coating thickness among all the coatings. The corrosion current density of the coated alloy was decreased by three orders of magnitude as compared to that of the bare alloy.

Key words: magnesium alloy; acid pretreatment; layered double hydroxide; intermetallic particles; steam coating; corrosion resistance

1 Introduction

Lightweight materials such as magnesium alloys have different distinguished properties such as high specific strength and stiffness, prominent process ability and biocompatibility, and hence they have gained high interest in the fields of aerospace, automobiles and biomedicine [1−5]. However, their high chemical reactivity and corrosion susceptibility hinder their widespread engineering and bio-implant applications [6−9]. Surface modification technologies such as layer-by-layer self-assembly coatings, chemical conversion and micro-arc oxidation (MAO) [10−14] are widely studied for developing high-performance coatings on Mg and its alloys. However, these treatments use chemicals in the preparation process, which are generally unfriendly to the environment. Hence, it is critical to develop an environment-friendly method, which is also simple and low-cost, for producing protective coatings with improved

anti-corrosion performance on Mg and its alloys.

Recently, layered double hydroxides (LDHs) have been extensively studied due to their possible applications in heterogeneous catalysts, thermal stability materials, anion exchangers, molecular sieves and composite coating [15−19]. It is important to note that due to its ion exchange capability, LDH can trap corrosive ions and thus retard corrosion reaction [20,21]. Therefore, LDH is considered as a promising material for improving the anti-corrosion performance of Mg alloys [22,23]. In previous work of our group, we combined co-precipitation and hydrothermal processes to prepare LDH coating on AZ31 Mg alloy, which provides good corrosion resistance [24−26]. Unfortunately, the process involved in producing such a coating is time-consuming.

Recently, ISHIZAKI et al [27] have prepared a LDH/Mg(OH)$_2$ coating on Mg alloys by a chemical-free steam coating method using ultrapure water. This in-situ steam method for developing LDH coating has good application prospects due to its simple operation and being environmentally friendly. In the in-situ steam process, the source of Al required for the coating growth only comes from the base material (AZ31 Mg alloy), thus limits the thickness and the film formation. Therefore, it is necessary to remove the oxides and activate the surface.

YANG et al [28] have studied the effect of coating pretreatment on tailoring the surface chemistry of AZ91D Mg alloy. In their research, alkaline conditioning and acid activation are the main pretreatment methods to control β-phase morphology and surface homogeneity. SHI et al [29] have reported that suitable alkali etching can accelerate the growth rate and improve the density of the anode film due to the modifications of microstructures (e.g. cathodic Al−Fe−Si−Mn phase, grain boundary and anodic Al−Mg−Si phase) with different local potentials from the matrix. NGUYEN et al [30] illustrated that the AZ91 Mg alloy was activated with a hydrofluoric acid solution prior to the zincification treatment to obtain a uniform zincate layer on the α and β phases, which leads to uniform electrodeposition of copper layer. ZENG et al [31] found that the size and distribution of Al−Mn phase particles in AZ31 and AM30 magnesium alloys can affect the microscopic morphology, roughness and anti-corrosion

performance of calcium-doped zinc phosphate coatings prepared on the surfaces, and that the Al−Mn phase plays a significant role in the process of coating film formation. Therefore, we speculate that Al−Mn phase plays a key role in the film formation stage of the LDH coating.

In AZ31 Mg alloy, the two main phases are α-Mg matrix and Al−Mn phase. Al is completely dissolved (solid solution) in α-Mg and hence there is no β-phase [32,33].

When AZ31 Mg alloy is immersed in acidic solution, many micro-galvanic corrosion cells will form on the surface due to the difference in the electrochemical properties of α-Mg phase and Al−Mn phase. In AZ31 Mg alloy, α-Mg phase takes the role of the anode, and Al−Mn phase acts as the cathode. In the micro-anode zones (α-Mg phase), Mg dissolves and in the micro-cathode zones (Al-Mn phase), hydrogen gas is produced. To the best of our knowledge, the effects of acid pretreatment on the exposure of intermetallic particles and its influence on in-situ Mg−Al−LDH steam coating of AZ31 Mg alloy have not yet been studied.

This research was aimed at fabricating a dense Mg−Al−LDH coating on AZ31 Mg alloy via an environmentally friendly treatment method, i.e. an acid pretreatment and a chemical-free steam method, and investigating the influence of the intermetallic Al−Mn particles on the formation of LDH coating.

2 Experimental

2.1 Fabrication of coating using steam

The preparation process of coating using steam as the medium is shown in Fig. 1. As-extruded AZ31 Mg alloy (composition: 1 wt.% Zn, 3 wt.% Al and balanced Mg) with a size of 20 mm × 20 mm × 5 mm, was used as the substrate material. The Mg alloy was polished with 2500 grit SiC papers, then cleaned with ethanol under ultrasonic environment and dried in air. The compositions of the acid pretreatment solution and the operation conditions are displayed in Table 1. For the acid pretreatment process, the polished magnesium alloy was firstly immersed in the prepared acid solutions for different periods, and then ultrasonically cleaned with deionized water. Subsequently, the Mg−Al−LDH coating was fabricated on the acid
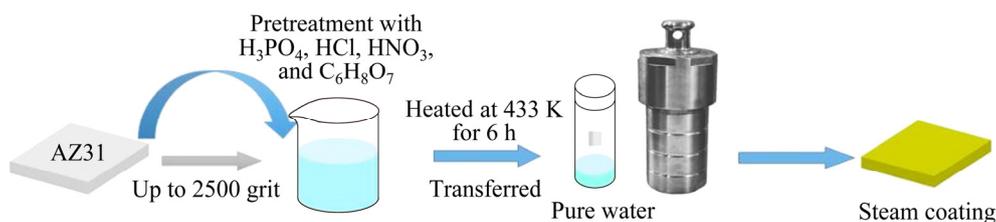
Fig. 1 Schematic diagram of preparation process for steam coating

Table 1 Pretreatment solutions and operation conditions at room temperature

Reagent	Formula	Concentration/ (mL·L^{-1})	pH	Time/ s
Phosphoric acid	H$_3$PO$_4$ (85%)	10	1.34	15
Hydrochloric acid	HCl (37%)	5	0.84	5
Nitric acid	HNO$_3$ (68%)	30	0.84	5
Citric acid	C$_6$H$_8$O$_7$ (s)	20*	1.34	15

* g/L

pretreated AZ31 samples through chemical-free steam method [27,34,35], where 20 mL of pure water was put into a Teflon-lined autoclave (100 mL) to produce steam. Then, the acid pretreated AZ31 sample was hung in the autoclave with a white thin cotton thread. There was a distance of approximately 3 cm between the substrate and water surface. The autoclave was slowly heated at a constant rate to 433 K, and then held for 6 h for the coating formation. The samples prepared with four different acid pretreatment solutions listed in Table 1 are designated as follows: H$_3$PO$_4$/LDH, HCl/LDH, HNO$_3$/LDH, and CA/LDH. The samples prepared on the polished AZ31 magnesium alloy surface are designated as LDH.

2.2 Surface characterization and phase analysis

The surface roughness (R_a) was measured using a Zeta−20 3D-morphology optical profile-meter. Based on over 5 values measured at different positions, the average roughness R_a was reported. The microstructure of Mg alloys was observed using an optical microscope (OM, Olympus-GX41, Japan). A field-emission scanning electron microscope (FE-SEM, Nova NanoSEM 450, USA) was used to observe surface morphologies of the coatings, at the same time, energy dispersive X-ray spectrometer (EDS) was used to characterize elemental composition of the coatings. Information on chemical bonding of the coatings was examined

by FT-IR (Nicolet 380, Thermo Electron Corporation, USA). X-ray diffractometer (XRD, Rigaku D/MAX2500PC, Japan) was adopted to evaluate the crystal microstructure of the coatings. Al−Mn phase surface area fraction analysis was performed using ImageJ software. The bonding of elements and chemical states of samples were investigated out on an X-ray photoelectron spectrometer (XPS, ESCALAB 250XI, Thermo Fisher Scientific, USA) with an Al K$_\alpha$ X-ray source, and the spectra were referenced to the adventitious C 1s peak (284.8 eV).

2.3 Electrochemical corrosion test

The anti-corrosion performance was estimated using a Princeton potentiostat (PARSTAT2273, Princeton Instruments Corporation, USA). All the test were conducted in 3.5 wt.% NaCl solution at room temperature. A three-electrode-cell with an exposed area of 1 cm^2 was used as the working electrode, a saturated calomel was used as the reference electrode and a platinum mesh was used as the counter electrode. The electrochemical impedance spectroscopy (EIS) measurements were performed in the frequency range from 100 kHz to 10 mHz with an amplitude disturbance of 5 mV. The potentiodynamic polarization curve was obtained from −2.0 to −0.5 V at a scanning rate of 1 mV/s. The EIS plots were fitted with the equivalent circuit model and analyzed by the ZSimpWin software. For the potentiodynamic polarization curves, corrosion current density (J_{corr}) and corrosion potential (φ_{corr}) were calculated by the Tafel extrapolation method. The polarization resistance R_p was obtained using Stern-Geary equation:

$$R_p = \beta_a\beta_c/[2.303J_{corr}(\beta_a+\beta_c)] \qquad (1)$$

where β_a and β_c are the positive and negative slopes of the potentiodynamic polarization curve, respectively.

2.4 Hydrogen evolution test

The hydrogen evolution test was conducted by placing the samples (fully exposed) in 3.5 wt.% NaCl solution at (25.0±0.1) °C under an inverted funnel connected to a graduated burette. The solution level in the burette was measured intermittently for 228 h. The hydrogen evolution rate (HER, mL/(cm^2·h)) can be associated with the immersion time, and they form a function as follows:

$$HER=V_H/(st) \tag{2}$$

where V_H is the hydrogen evolution volume (mL), s and t are the exposed area (cm^2) and immersion time (h), respectively.

2.5 Salt spray test

The anti-corrosion performance of the sample was accessed by a salt spray test. The experiment was conducted in a continuous spray mode, and the concentration of the NaCl solution was 5 wt.%. The room temperature and saturator temperature of the salt spray experiment box were set to be 35 and 47 °C, respectively. The samples were taken out after 3, 6, 12 and 24 d exposure and observed for corrosion attack, and images were captured using a digital camera.

3 Results

3.1 Microstructure and chemical compositions of coating

Figure 2 shows the optical microstructures of polished AZ31 and pretreated alloy with 4% nitric acid alcohol, H$_3$PO$_4$, HCl, HNO$_3$, and CA. As seen in Fig. 2(a), there are small amount of Al−Mn phase particles on the polished AZ31 surface. The 4% nitric acid used here is a commonly used metallurgical etching solution for AZ31 Mg alloy. Figure 2(b) reveals the grain boundaries, but the number of Al−Mn phase particles is relatively small. There are no obvious grain boundaries in Figs. 2(c−f) as compared to in Fig. 2(b). In Figs. 2(c) and (d), due to the severe corrosion that occurs during the acid pretreatment corrosion, the Al−Mn phase falls off and leaves many corrosion pits on the surface of H$_3$PO$_4$/AZ31 and HCl/AZ31. Figure 3 shows the corresponding Al−Mn phase surface area fractions for different samples in Fig. 2. We determined the second phase surface area fraction by calculating the area of the pits. Although a higher surface area fraction is seen in Fig. 3, the second phase has fallen off. Therefore, the H$_3$PO$_4$ and HCl pretreatments have an inhibitory effect on increasing the surface area fraction of the Al−Mn phase. The microstructures in Figs. 2(e) and (f) comprise α-Mg phase and a considerable amount of Al−Mn phase. As we can see in Fig. 3, the surface area fraction of the Al−Mn phase increases up to about two times for the HNO$_3$-pretreated AZ31 and about three times for the CA-pretreated AZ31 as compared to the polished AZ31 Mg alloy. This shows that proper acid pretreatment can alter the distribution density of second phase particles on the substrate surface.
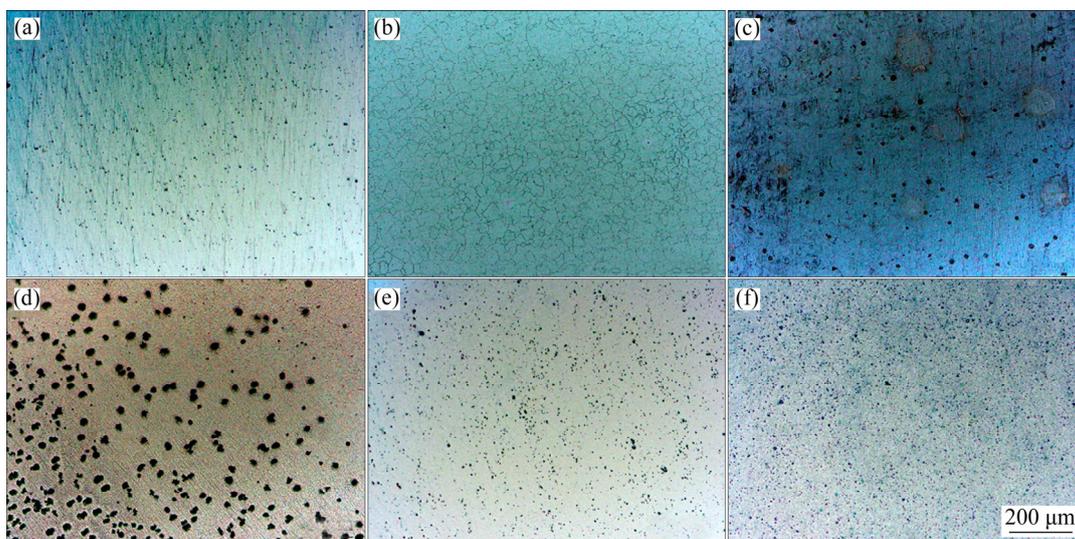

Fig. 2 Optical microstructures of polished AZ31 (a), AZ31 pretreated with 4% nitric acid alcohol (4% nitric acid alcohol/AZ31) (b), AZ31 pretreated with H$_3$PO$_4$(H$_3$PO$_4$/AZ31) (c), AZ31 pretreated with HCl(HCl/AZ31) (d), AZ31 pretreated with HNO$_3$(HNO$_3$/AZ31) (e) and AZ31 pretreated with CA(CA/AZ31) (f)
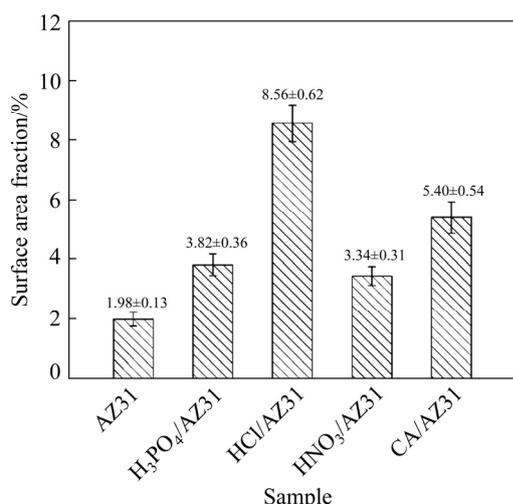
Fig. 3 Al−Mn phase surface area fractions corresponding to different samples in Fig. 2

The effects of four activation agents were studied in this work (Table 1). The surface morphologies and corresponding elemental compositions of polished AZ31, H_3PO_4/AZ31, HCl/AZ31, HNO_3/AZ31 and CA/AZ31 are displayed in Fig. 4 and Table 2, respectively. The surface 3D-morphologies and roughness information after various acid activations are given in Fig. 5 and Fig. 6, respectively. As can be observed, there are no obvious Al−Mn phase (Spectrum $2^\#$) on the AZ31 Mg alloy surface, which may be due to the hindrance of the oxide and hydroxide layers on the magnesium alloy surface. The activation of H_3PO_4 partially dissolved the matrix and the generated insoluble corrosion products of magnesium phosphate (Spectrum $3^\#$), resulting in an increased roughness as compared to the polished AZ31 (Fig. 4(b)). Through the activation with HCl, significant uniform corrosion was observed (Fig. 4(c)), corresponding to a smaller surface roughness. With the activation of HNO_3, uniform corrosion occurred and the α-Mg phase dissolved to form a prominent Al−Mn phase (Al_8Mn_5 and AlMn) as displayed in Fig. 4(d) (Spectra $7^\#$ and $8^\#$). Following etching in CA solution, the microstructure is similar to that of nitric acid, but the surface is smoother except the fact that the Al−Mn phase (Al_8Mn_5 and AlMn) remains prominent in Fig. 4(e) (Spectra $9^\#$ and $10^\#$). It is worth noting that, as compared with the polished AZ31 Mg alloy, the exposed Al−Mn phase can be clearly observed on the surface of AZ31 pretreated with HNO_3 and CA, and the quantity has

significantly increased. This provides a large number of growth sites for the subsequent growth of the LDH coating, which has a positive effect on the growth process of the coating. Accordingly, the roughness can be arranged in an ascending order as follows: polished AZ31 ((0.79±0.03) μm) < HCl/AZ31 ((0.84±0.02) μm) < H_3PO_4/AZ31 ((0.94±0.07) μm) < CA/AZ31 ((0.95±0.02) μm) < HNO_3/AZ31 ((1.02±0.07) μm), which was in keeping with the surface morphology images in Fig. 4.

Figure 7 and Table 3 show the surface morphologies and corresponding elemental compositions of the steam coating. Figure 7(c) exhibits that the growth of the obtained ordinary steam coating on the whole AZ31 substrate is relatively dense. Figure 7(a) shows that the H_3PO_4/LDH has a curved sheet-like structure on the surface, which is loose and porous. The surface of the HCl/LDH is covered with a layer of substance (mainly composed of $Mg(OH)_2$) in comparison with the LDH coating in Fig. 7(b). However, the surface morphology of the HNO_3/LDH and CA/LDH coating is much more compact than that of the LDH coating. Besides, the size of vertically grown nanoplates is smaller, and the gap between the LDH nanoplates is also smaller. In addition, it is noteworthy to see that the CA/LDH coating is the densest among all the samples studied here, which illustrates that CA pretreatment has the best effect on the growth of the LDH coating.

Table 3 shows elemental compositions for steam coating and acid-pretreated steam coating. The data in Table 3 indicate that the steam coating (corresponding to Spectra $7^\#-9^\#$ in Fig. 7(c)) primarily contains O, Mg, Al and C elements, in which the contents of Mg and O are relatively high, proving the existence of Mg−Al−LDH and $Mg(OH)_2$ on the magnesium alloy substrate. And the data demonstrate that Mg, Al and C contents of the steam coating after HNO_3 and CA pretreatment (corresponding to Spectra $10^\#-15^\#$ in Figs. 7(d) and (e)) are higher than those of the ordinary LDH coating, while the O content is relatively low. This indicates that the content of LDH in HNO_3/LDH and CA/LDH steam coatings is much more higher than that of the ordinary LDH coating. The above results show that proper acid pretreatment has an useful effect on the growth of the in-situ steam coating.
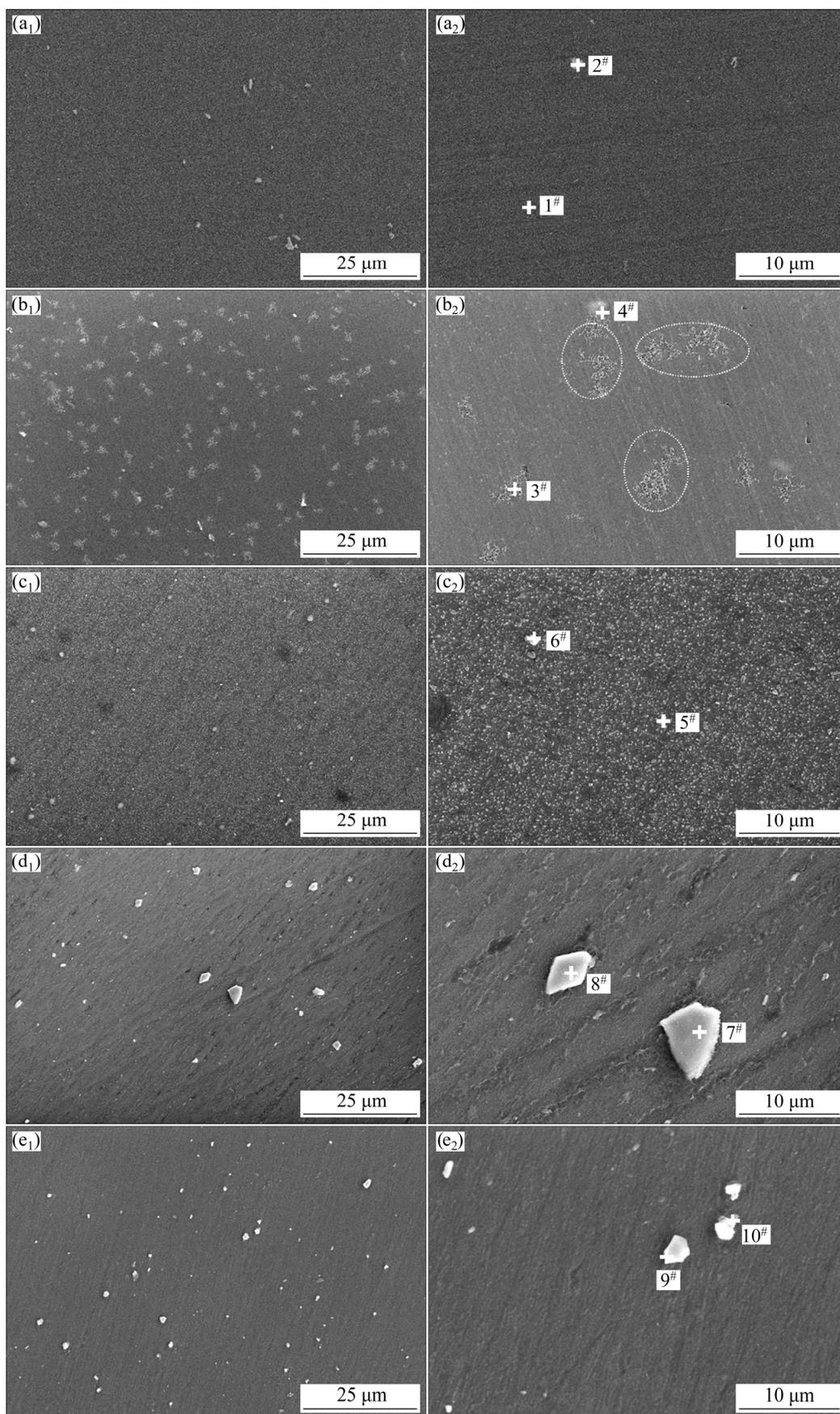
Fig. 4 FE-SEM images of polished AZ31 substrate (a_1, a_2), H_3PO_4/AZ31 coating (b_1, b_2), HCl/AZ31 coating (c_1, c_2), HNO_3/AZ31 coating (d_1, d_2) and CA/AZ31 coating (e_1, e_2)

Table 2 Elemental compositions of selected spectra on LDH coating as shown in Fig. 4 (at.%)

| Spectrum No.	Mg	O	Al	Cl	Mn	P	Al/Mn molar ratio
1#	98.66	−	1.15	−	0.19	−	−
2#	69.30	−	20.80	−	9.85	−	−
3#	92.64	5.24	1.70	−	0.11	0.31	−
4#	89.86	5.45	3.39	−	0.69	0.62	−
5#	86.03	10.69	3.24	−	0.05	−	−
6#	86.57	9.75	3.09	0.11	0.48	−	−
7#	−	−	60.46	−	39.54	−	8/5
8#	−	−	50.28	−	49.72	−	1/1
9#	−	−	49.10	−	50.90	−	1/1
10#	−	−	63.53	−	36.47	−	9/5
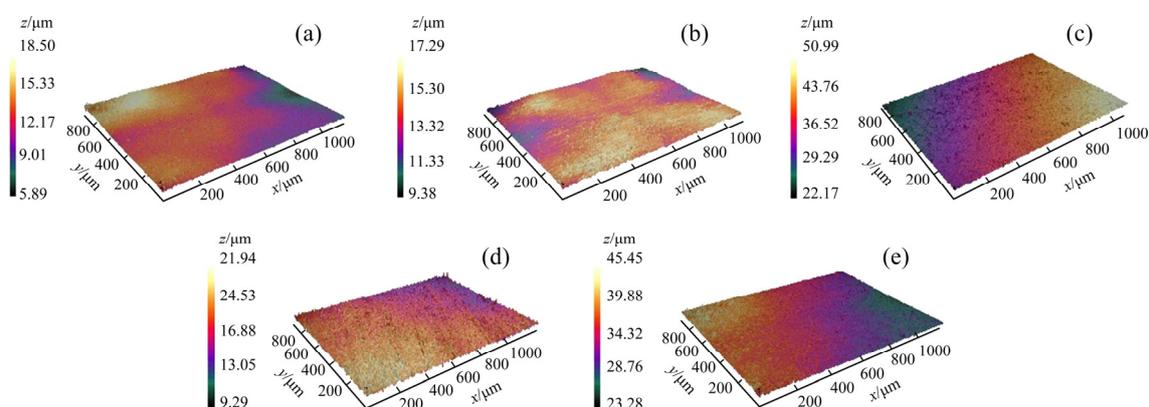
Fig. 5 Surface 3D-morphologies of AZ31 Mg alloy after activation by various acids: (a) Polished AZ31 substrate; (b) H_3PO_4/AZ31 coating; (c) HCl/AZ31 coating; (d) HNO_3/AZ31 coating; (e) CA/AZ31 coating
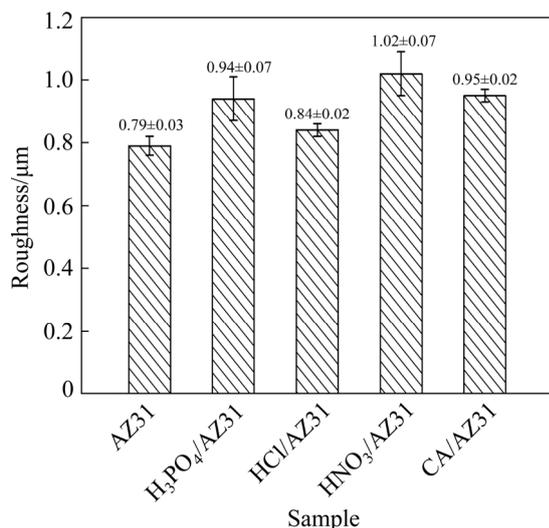
Fig. 6 Roughness corresponding to different samples in Fig. 5

Figure 8 demonstrates cross-sectional micro-structures as well as relevant elemental mapping images of H_3PO_4/LDH, HCl/LDH, LDH, HNO_3/LDH and CA/LDH coatings. For H_3PO_4/LDH and HCl/LDH coatings, it is not difficult to see that the LDH coating is not combined closely with the AZ31 Mg alloy. In addition, cracks are apparent, as in the white circles in Figs. 8(a) and (b), which suggests that the coating is relatively loose. The reason is that H_3PO_4 and HCl pretreatments change the surface morphologies of the AZ31 substrate, and the corrosion products cover the Al−Mn phase on the magnesium alloy surface in Figs. 2(c) and (d) and increase the difficulty of the growth of the LDH coating. For HNO_3/LDH and CA/LDH coatings, the coating is denser and firmly bonded on the AZ31 Mg alloy. The thickness of the coating is in the following ascending order: H_3PO_4/LDH ((26.46±0.68) μm) < HCl/LDH ((29.84±0.31) μm) < LDH ((30.85±0.96) μm) < HNO_3/LDH ((34.25± 0.50) μm) < CA/LDH ((37.65±0.46) μm).

The diffraction peaks of the acid pretreated steam coating and the ordinary steam coating shown in Fig. 9 indicate that LDH coating is successfully formed on the alloy. The two peaks at $2\theta \approx 11.3°$ and 22.6° correspond to the (003) and (006) diffraction peaks of $Mg-Al-CO_3^{2-}-LDH$ [36]. The characteristic peaks of $Mg(OH)_2$ at 2θ about 18.4°, 37.9°, 58.2° and 62.8° are also shown in
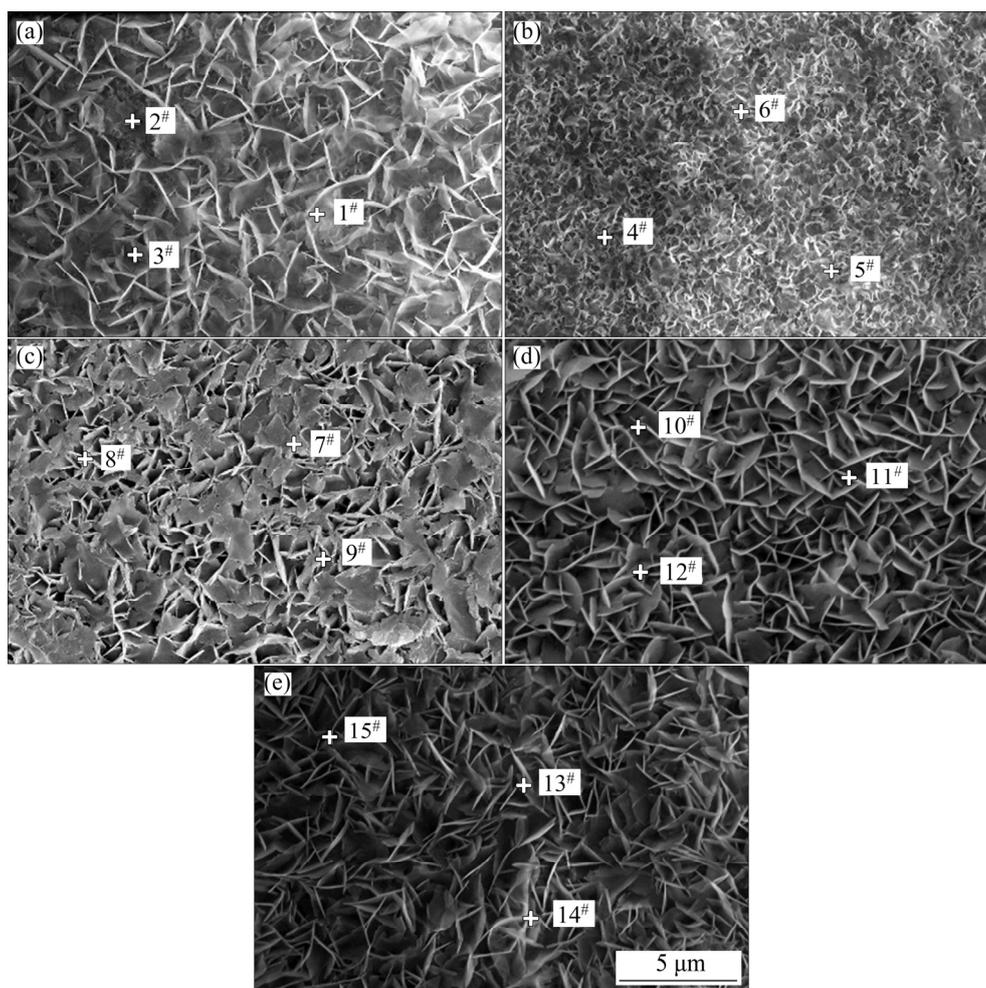
Fig. 7 FE-SEM images of H₃PO₄/LDH (a), HCl/LDH (b), LDH (c), HNO₃/LDH (d) and CA/LDH (e) coatings

Table 3 Elemental compositions of LDH coating as shown in Fig. 7 (at.%)

Sample	Mg	O	Al	C
LDH	31.72±0.53	64.18±0.88	1.51±0.08	2.60±0.43
H₃PO₄/LDH	33.40±0.75	64.55±0.92	1.03±0.01	1.02±0.18
HCl/LDH	32.76±0.61	64.62±0.64	1.11±0.01	1.52±0.03
HNO₃/LDH	37.84±1.36	56.40±1.35	2.09±0.21	3.67±0.19
CA/LDH	38.25±2.07	55.22±2.01	2.62±0.37	3.91±0.43

Fig. 9 [37]. These results demonstrate that the mixed structure of $Mg(OH)_2$ and $Mg-Al-CO_3^{2-}$ LDH phases forms the film coated on AZ31. The formation of $Mg(OH)_2$ is due to the preferential reaction of water vapor with the dissolved Mg^{2+} ions during the reaction process. It is noteworthy that the intensities of the diffraction peaks for the LDH coating pretreated by four kinds of acid here are significantly different. As observed, the CA/LDH coated sample possessed the strongest diffraction peak of LDH phase, indicating relatively

high content of LDH compared to other samples investigated here, which was consistent with the surface morphologies and cross-sectional results shown in Figs. 7(e) and 8(e).

3.2 Corrosion behavior

Figure 10 exhibits the potentialdynamic polarization curves of all samples. Table 4 shows the corrosion current density (J_{corr}) and corrosion potential (φ_{corr}) of all coatings acquired by the Tafel curve extrapolation method. We can know that
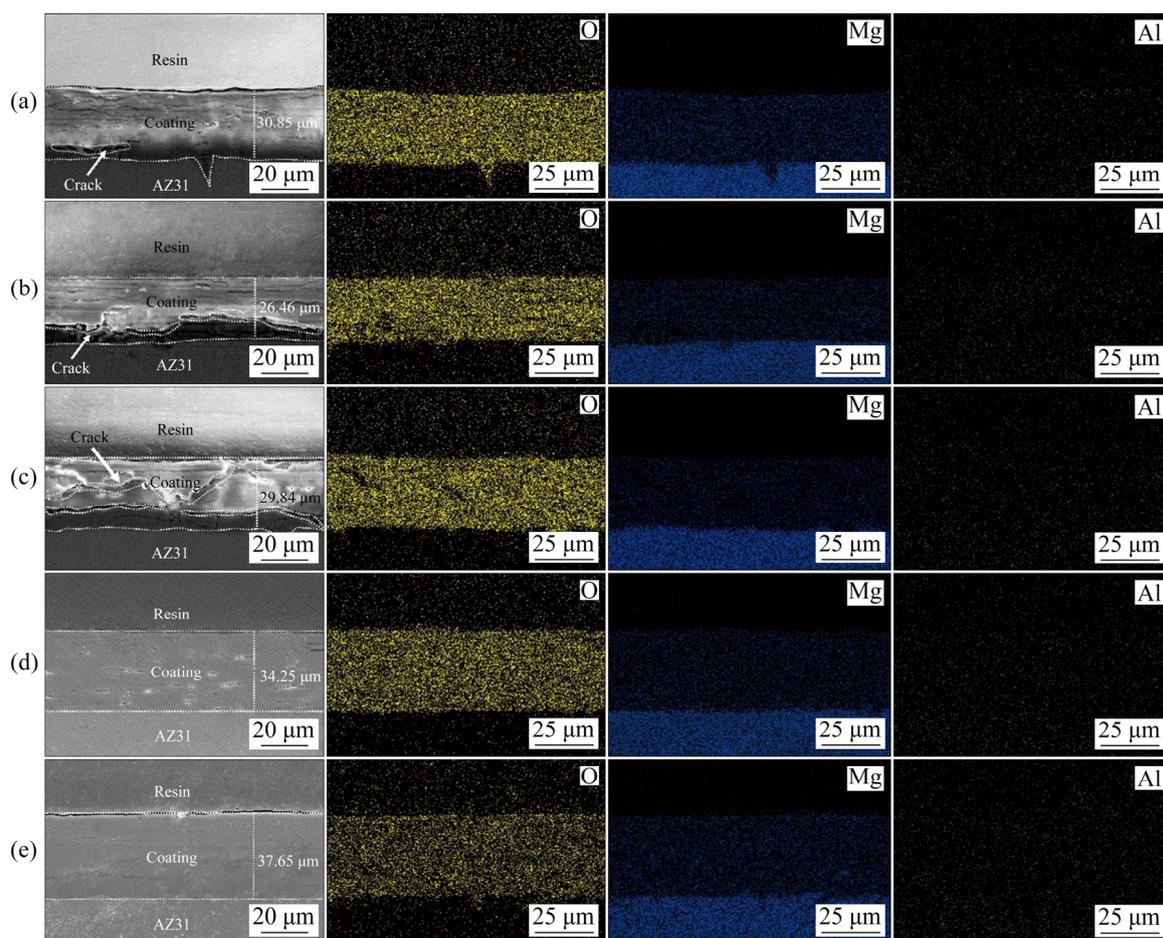
Table 4 Electrochemical parameters of polarization curves of samples

Sample	φ_{corr}(vs SCE)/V	J_{corr}/(A·cm^{-2})	β_a/(mV·dec^{-1})	$-\beta_c$/(mV·dec^{-1})	R_p/(Ω·cm^2)
AZ31	−1.46	$1.42×10^{-5}$	51.62	66.87	$8.47×10^3$
H$_3$PO$_4$/LDH	−1.46	$5.32×10^{-7}$	108.28	91.78	$4.05×10^4$
HCl/LDH	−1.36	$4.54×10^{-7}$	110.35	93.80	$5.08×10^4$
LDH	−1.31	$4.22×10^{-7}$	127.99	112.17	$6.15×10^4$
HNO$_3$/LDH	−1.31	$2.21×10^{-7}$	196.70	119.56	$2.86×10^5$
CA/LDH	−1.28	$4.46×10^{-8}$	269.25	139.16	$1.24×10^6$

values increased when compared with that of the LDH coating. At the same time, the φ_{corr} value of CA/LDH is more positive than that of the LDH coating, and the corresponding J_{corr} values decrease by contrast with that of the LDH coating, suggesting that both HNO$_3$/LDH and CA/LDH coatings could enhance the anti-corrosion performance of LDH coating. In addition, the increasing order of the polarization resistance (R_p) for different samples is AZ31 substrate < H$_3$PO$_4$/LDH coating < HCl/LDH coating < LDH coating < HNO$_3$/LDH coating < CA/LDH coating. Notably, the J_{corr} of CA/LDH is about one order of magnitude lower than that of LDH, and three orders of magnitude lower than that of the substrate. Therefore, among all the samples, the CA/LDH coating has the best anti-corrosion performance.

Figure 11 shows the EIS spectra of AZ31 substrate and LDH coatings in 3.5 wt.% NaCl solution. From Fig. 11(a), in the low frequency region, |Z| modulus of all samples can be arranged in an ascending order as follows: AZ31 substrate < H$_3$PO$_4$/LDH coating < HCl/LDH coating < LDH coating < HNO$_3$/LDH coating < CA/LDH coating. In general, a higher |Z| modulus at lower frequencies indicates that the coating owns a better corrosion resistance. Therefore, the CA/LDH coating has the best anti-corrosion performance. Bode phase plots of all coatings in Fig. 11 are composed of two time constants, which correspond to the multilayer structure, namely, barrier inner-layer and the porous outer-layer, respectively [26]. At the same time, for the LDH-coated samples in Figs. 11(c−f), there are two capacitive loops due to two structural layers of LDH coating. The curvature radius of CA pretreatment steam coating sample is much larger as compared with that of other samples, indicating that CA-pretreated sample possess the optimum corrosion protection performance. Thus,

appropriate acid pretreatment can remarkably enhance anti-corrosion performance of the steam coating.

Figures 11(g) and (h) display disparate equivalent circuit (EC) diagrams corresponding to the EIS results. Table 5 shows the corresponding fitting data of Fig. 11(h). Figure 11(g) exhibits the EC of the AZ31 Mg alloy. The high-frequency region is constituted by interface diffusion constant phase components (CPE$_3$) and charge transfer resistance (R_{ct}), indicating that a loose porous corrosion product film is formed on the AZ31 Mg alloy. R_f is film resistance, R_s is the solution resistance and CPE$_1$ is the film capacitance which is ascribed to electrolyte penetrating via the corrosion product layer on the substrate surface. The low-frequency region consists of the resistance (R_L) and inductance (L), which means the pitting corrosion of the AZ31 substrate. The fitted data for the AZ31 substrate are: R_s=33.79 Ω·cm^2, CPE$_1$= $1.27×10^{-5}$ Ω^{-1}·s^n·cm^{-2}, n_1=0.82, R_f=57.12 Ω·cm^2, CPE$_3$=$3.4×10^{-6}$ Ω^{-1}·s^n·cm^{-2}, n_3=0.96, R_{ct}=3.0× 10^3 Ω·cm^2, R_L=$2.66×10^4$ Ω·cm^2, and L=3.29× 10^5 H·cm^{-2}. The LDH coatings with and without acid pretreatment show similar Nyquist plots, and one equivalent circuit can be fitted in Fig. 11(h). The circuit includes R_{ct}, R_s, R_1, R_2, CPE$_3$, as well as the porous outer-layer capacitance (C) and the barrier inner-layer capacitance (CPE$_2$). Among them, the resistances of the outer-layer and inner-layer of the Mg−Al−LDH coating are represented by R_1 and R_2, respectively. In addition, a higher R_{ct} value indicates a better anti-corrosion performance. The R_{ct} value of CA/LDH coating is the largest in all the samples researched here (Table 5), manifesting the strongest protection to the substrate.

Figure 12 displays curves of hydrogen evolution rate (HER) values for the substrate and
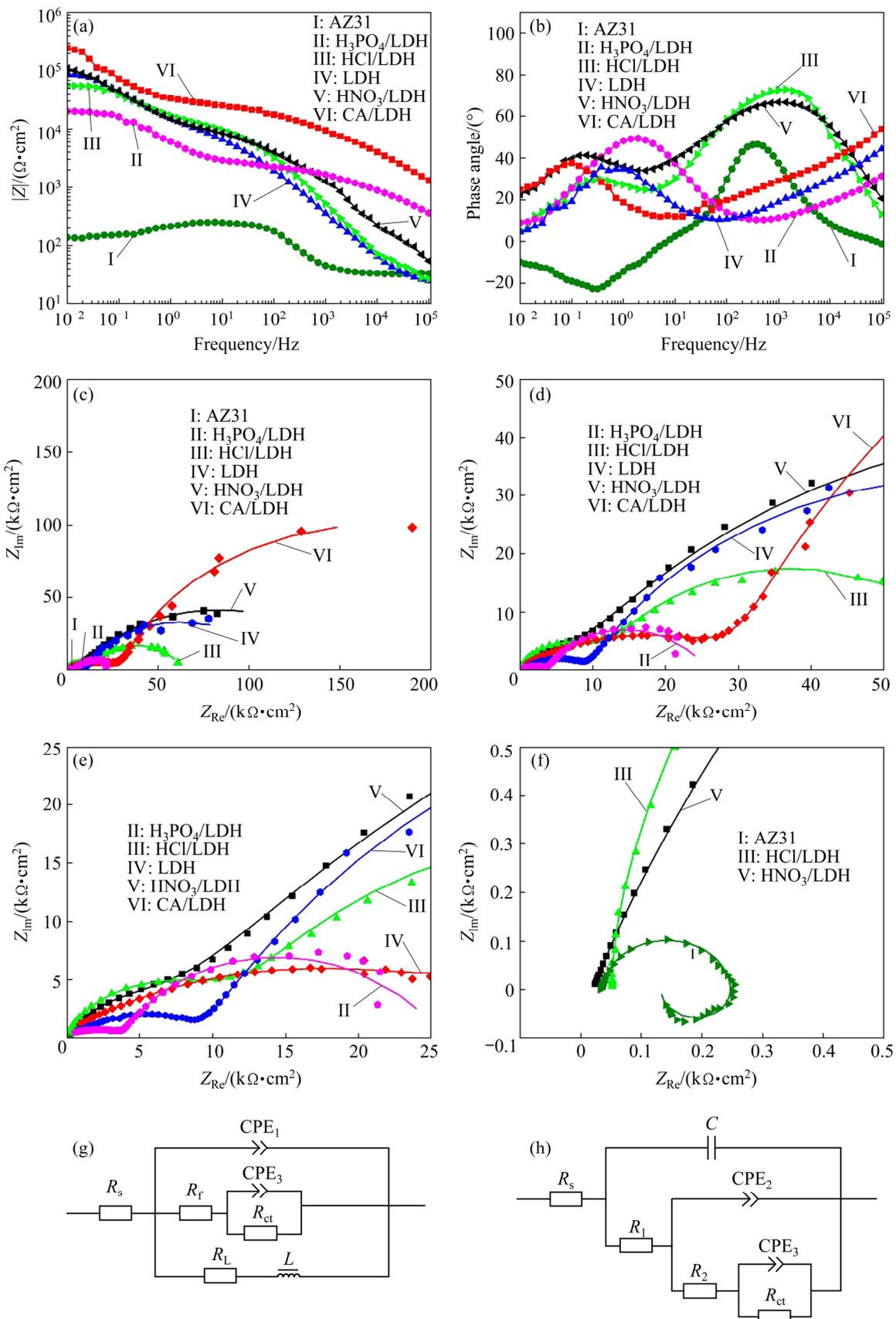
Fig. 11 EIS data of AZ31 substrate, H₃PO₄/LDH, HCl/LDH, LDH, HNO₃/LDH and CA/LDH coatings: (a) Bode plots of |Z| vs frequency; (b) Bode plots of phase angle vs frequency; (c) Nyquist plots; (d−f) Enlarged Nyquist plots; (g, h) Equivalent circuits of AZ31 substrate and LDH coatings, respectively

Table 5 EIS data recorded in Fig. 11

Sample	R_s/ ($\Omega \cdot cm^2$)	C/ ($F \cdot cm^{-2}$)	R_1/ ($\Omega \cdot cm^2$)	CPE_2/ ($\Omega^{-1} \cdot s^n \cdot cm^{-2}$)	n_2	R_2/ ($\Omega \cdot cm^2$)	CPE_3/ ($\Omega^{-1} \cdot s^n \cdot cm^{-2}$)	n_3	R_{ct}/ ($\Omega \cdot cm^2$)
H_3PO_4/LDH	77.27	1.68×10^{-9}	4.13×10^{-2}	6.22×10^{-6}	0.43	3.9×10^3	4.19×10^{-5}	0.75	2.17×10^4
HCl/LDH	51.46	2.76×10^{-7}	1.68×10^2	2.98×10^{-6}	0.65	1.21×10^4	2.71×10^{-5}	0.74	5.05×10^4
LDH	74.61	1.14×10^{-8}	3.59×10^2	5.75×10^{-6}	0.56	9.86×10^3	4.65×10^{-6}	0.91	7.55×10^4
HNO_3/LDH	40.12	7.08×10^{-8}	8.08×10^2	5.86×10^{-6}	0.55	1.25×10^4	2.25×10^{-5}	0.81	1.07×10^5
CA/LDH	61.36	5.29×10^{-10}	1.41×10^2	2.02×10^{-6}	0.42	3.40×10^4	2.06×10^{-5}	0.81	3.07×10^5
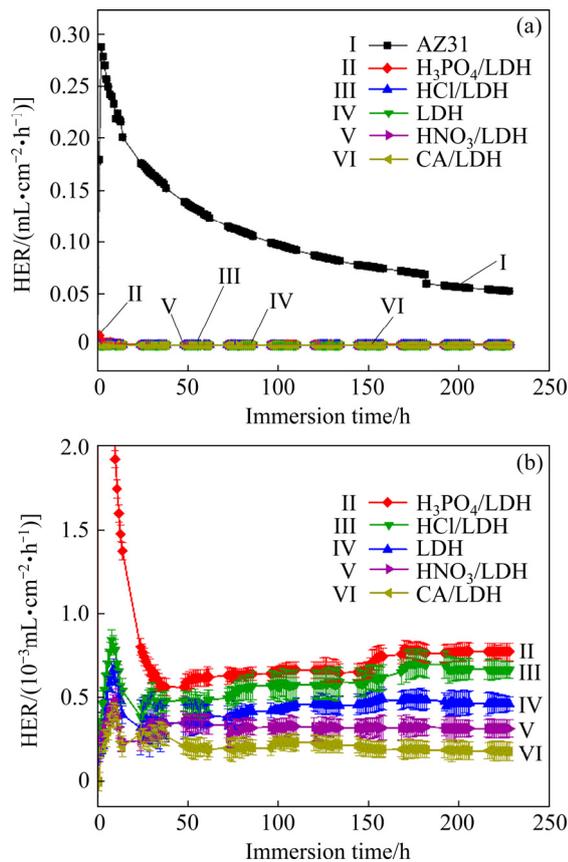
Fig. 12 HER as function of immersion time for AZ31 substrate, and H_3PO_4/LDH, HCl/LDH, LDH, HNO_3/LDH and CA/LDH coatings in 3.5 wt.% NaCl solution for 228 h

the LDH coatings with and without acid pretreatment in 3.5 wt.% NaCl solution for 228 h. As can be seen in Figs. 12(a) and (b), the HER of the substrate is much higher than that of the coated sample in the initial immersion stage. When the immersion time reaches approximately 3 h, the HER of the AZ31 substrate drops drastically due to the dissolution of Mg alloy and the formation of $Mg(OH)_2$ precipitate. With increasing the immersion time, the HER curve of the AZ31 substrate became smooth due to the protection of the corrosion products deposited on the substrate

surface. It is noteworthy that there is a slight increase after 50 h in HER for the H_3PO_4/LDH, HCl/LDH and LDH coatings, indicating that the coatings deteriorate during immersion in the corrosive media. The HER of the HNO_3/LDH and CA/LDH coatings shows a decreasing trend and levels after 35 h, which means better long-term corrosion protection. This can give the credit to the protection of the corrosion product film formed on the coating surface. The HER results of the CA/LDH coating have been kept to the lowest level during the entire immersion process, manifesting that the CA/LDH coating has the best protection effect on the substrate in the long term.

Figures 13(a_1−f_1) and (a_2−f_2) show the digital camera photographs and SEM images of AZ31 substrate and LDH coatings with and without acid pretreatment after 228 h of immersion in 3.5 wt.% NaCl solution, respectively. In Figs. 13(a_1−f_1), the AZ31 is severely corroded, and large corrosion pits appear on the H_3PO_4/LDH and HCl/LDH surfaces, small corrosion pits appear on the LDH and HNO_3/LDH surfaces, while only the CA/LDH surface has no obvious corrosion pits. It is not difficult to see from Fig. 13(a_2) that the AZ31 substrate surface is seriously damaged after immersion. Figure 13(c_2) shows that the morphology of the H_3PO_4/LDH on the surface completely disappeared as compared with the original sample (Fig. 7(b)). As for the HCl/LDH coating in Fig. 13(d_2), there are corrosion pits on the surface. Compared with the original sample shown in Fig. 7(c), the morphology has changed. For the LDH coating without acid pretreatment, a small number of corrosion pits appear on the surface and the surface morphology changes completely, indicating that the LDH coating is degraded and covered by corrosion products. The surface of HNO_3/LDH coating is partially covered by corrosion products and retains part of the LDH
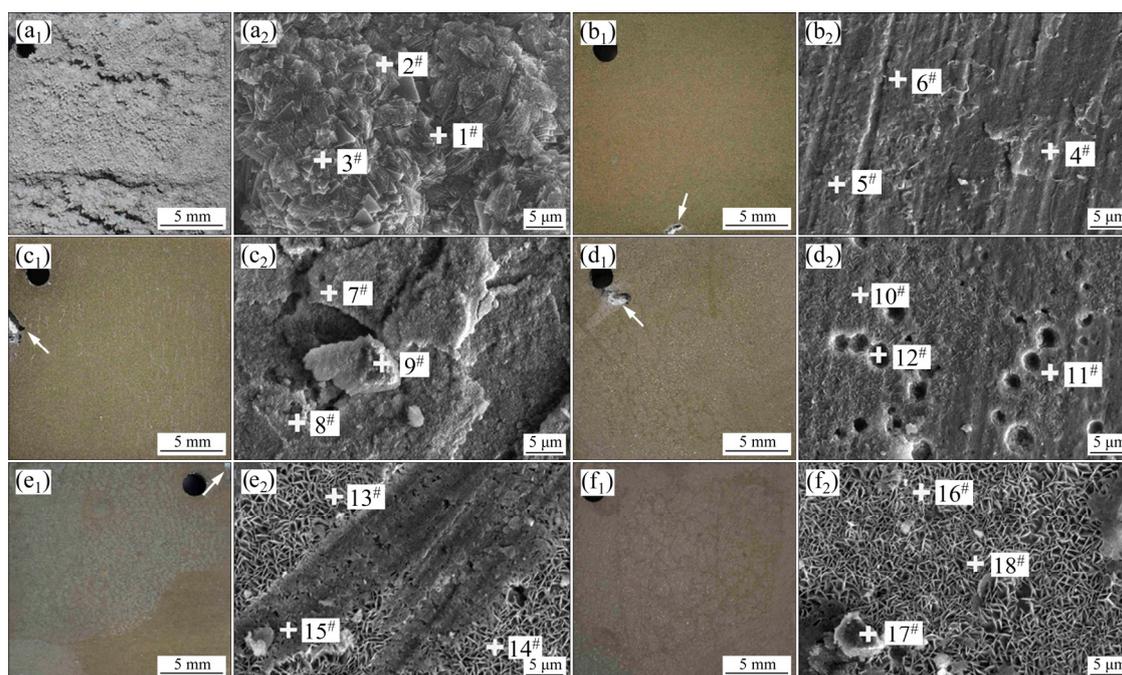
Fig. 13 Digital camera photographs (a_1−f_1) and FE-SEM images (a_2−f_2) of AZ31 substrate (a_1, a_2), LDH (b_1, b_2), H_3PO_4/LDH (c_1, c_2), HCl/LDH (d_1, d_2), HNO_3/LDH (e_1, e_2) and CA/LDH (f_1, f_2) coatings after immersion in 3.5 wt.% NaCl solution for 228 h

morphology. It should be noted that there are no obvious cracks in the CA/LDH coating and no major changes in surface morphology, suggesting good anti-corrosion performance. The corresponding element contents are shown in Table 6. It is noteworthy that the molar fractions of O and Mg in all samples are very high, which indicates that the corrosion products are mainly $Mg(OH)_2$. For H_3PO_4/LDH and HCl/LDH coatings, the C, O and Al contents are the lowest, while Mg content is the highest, which means severe corrosion. In addition, for HNO_3/LDH and CA/LDH coatings, the C and Al contents are higher, indicating slight corrosion. Finally, the morphology of CA/LDH is not affected, manifesting the best anti-corrosion performance of the coating.

Table 6 Elemental compositions corresponding to different samples in Fig. 13 (at.%)

Sample	Al	C	Mg	O
AZ31	0	5.67	25.62	68.71
LDH	1.54	6.34	26.78	65.34
H_3PO_4/LDH	1.04	6.64	28.98	63.34
HCl/LDH	1.22	7.81	29.42	61.55
HNO_3/LDH	3.15	12.76	12.21	71.88
CA/LDH	4.16	13.33	10.7	71.81

In order to further explore the long-term anti-corrosion performance of each sample, salt spray testing and analysis were performed. Figure 14 shows the digital camera photos of each sample placed in 5 wt.% NaCl salt spray environment for different durations. After 72 h of exposure, the surface of AZ31 was severely corroded and covered by corrosion products. A small number of corrosion pits appeared on the edge of the LDH coating, while the number and size of the corrosion pits at the edge of H_3PO_4 and HCl/LDH were significantly larger. It is noteworthy that the surface of HNO_3/LDH and CA/LDH had no obvious change. The number of corrosion pits on the LDH surface, H_3PO_4/LDH and HCl/LDH samples increased when the exposure time reached 144 h. Among them, the severest corrosion occurred on the surface of H_3PO_4/LDH and HCl/LDH, and a small number of corrosion pits appeared on the surface of HNO_3/LDH, while the surface of CA/LDH remained unchanged. When the exposure time reached 288 h, corrosion pits appeared on the surfaces of all the samples. The surface of CA/LDH had the least number of corrosion pits, showing its best long-term corrosion protection. When the exposure time reached 576 h, the number and size
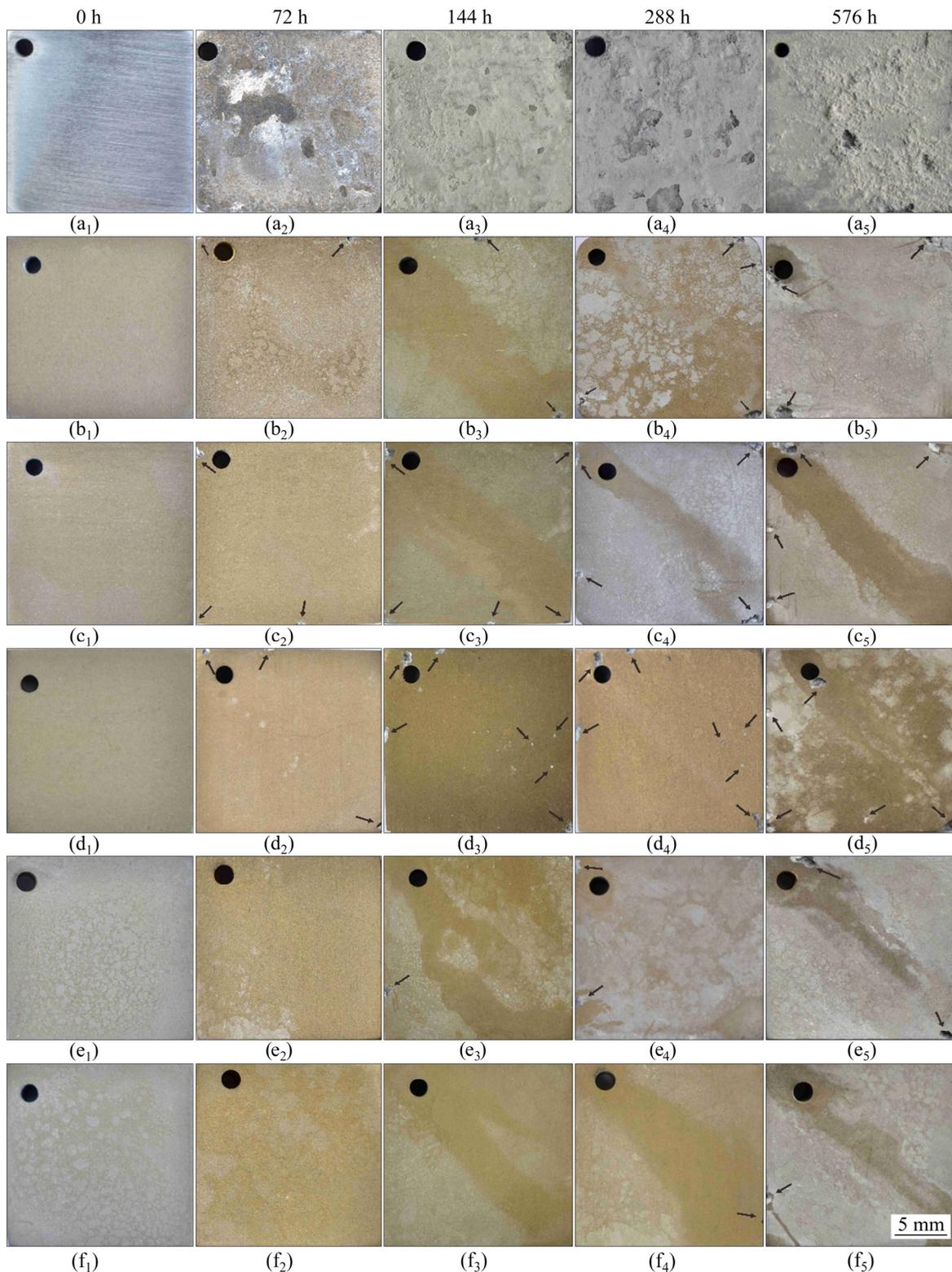
Fig. 14 Digital camera photographs of AZ31 substrate (a₁−a₅), and LDH (b₁−b₅), H₃PO₄/LDH (c₁−c₅), HCl/LDH (d₁−d₅), HNO₃/LDH (e₁−e₅) and CA/LDH (f₁−f₅) coatings in salt spray environment of 5 wt.% NaCl for different time

of corrosion pits on the surfaces of all the samples increased and the surfaces of the samples were covered with a plentiful of white corrosion products. It was not difficult to see that there was less corrosion pits on the CA/LDH surface (Fig. 14(f₅)). Therefore, it can be concluded that CA/LDH can provide the best long-term protection to the substrate. It was noted in Fig. 14(d₃) that pitting

occurred on the HCl/LDH surface, which may be due to the residual Cl⁻ ions resulting from the pretreatment process. The presence of corrosive Cl⁻ ions can easily lead to pitting corrosion of magnesium alloy.

Figures 15(a−e) show the cross-sectional micro-structures of samples after 576 h of salt spray testing. For the coating investigated here, the thickness of all coatings was reduced, and can be arranged in the following order: H_3PO_4/LDH (11.91 μm) < HCl/LDH (17.57 μm) < LDH (19.13 μm) < HNO_3/LDH (22.34 μm) < CA/LDH (25.49 μm). The coating structure can be clearly divided into the outer layer and inner layer, which have similar elemental composition as shown in Figs. 15(f, g). It can be concluded from the elemental composition that the outer layer is principally composed of $Mg(OH)_2$, and the inner layer is LDH. From Figs. 15(a−d), it can be seen that many micro-cracks appeared throughout the whole coating. In the corrosive medium, the corrosive ions reached the substrate surface through the cracks, and then galvanic corrosion occurred, which eventually led to the separation of the coating from the substrate. However, it is noteworthy that the CA/LDH coating in Fig. 15(e) is relatively intact and unaffected, with only some horizontal cracks. In the corrosive media, an ion exchange reaction occurred between the LDH layer and the Cl⁻ ions, and then the CO_3^{2-} of the LDH coating reacted with the Mg^{2+} ions generated by the dissolution of the coating at the coating/solution interface to form $MgCO_3$ which was converted into $Mg(OH)_2$ under alkaline conditions. The presence of $Mg(OH)_2$ layer protected the coating and prevented further corrosion, indicating that the LDH/$Mg(OH)_2$ coating had self-healing ability, which corresponded to the passivation area in the anode area of the polarization curves in Figs. 10(b−f).
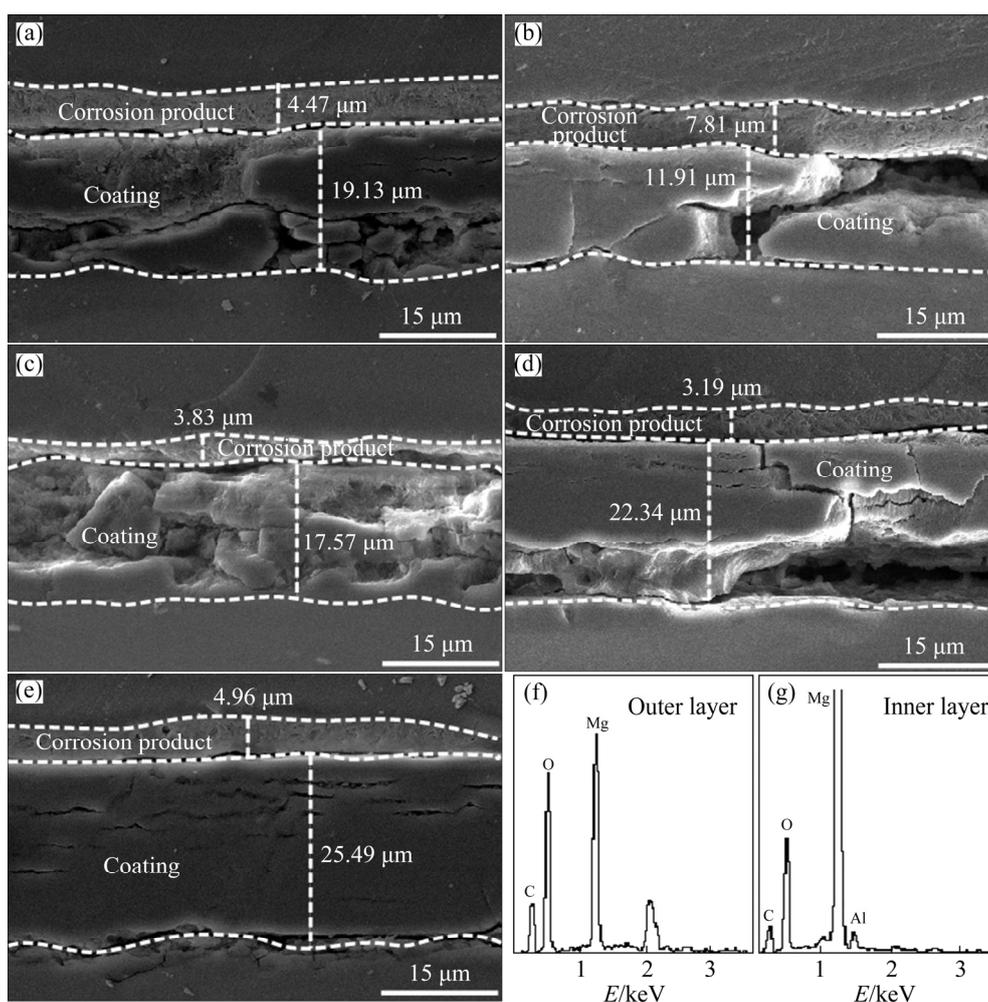

Fig. 15 Cross-sectional microstructures of LDH (a), H_3PO_4/LDH (b), HCl/LDH (c), HNO_3/LDH (d) and CA/LDH (e) coatings in salt spray environment of 5 wt.% NaCl for 576 h, and corresponding element compositions of outer (f) and inner (g) layers

4 Discussion

4.1 Effect of acid pretreatment time on surface area fraction of Al−Mn phase

Figure 16 shows the optical micrographs of the AZ31 surface after four kinds of acid pretreatment for different time. From Figs. 16(a₁−a₄) and (b₁−b₄), it is apparent that the quantity of the corrosion pits on AZ31 Mg alloy surface grows with the increase in the pretreatment time. Corrosion products and cracks were observed on the surfaces of H₃PO₄/AZ31-45 s and HCl/AZ31-20 s samples, as shown in Figs. 16(a₅) and (b₅) highlighted with the white circles. The high P and Cl contents (Table 7

(Spectra 2# and 4#)) in the corrosion products suggest that they are mainly magnesium phosphate and magnesium chloride, respectively. Therefore, it can be concluded that H₃PO₄ and HCl pretreatments have a negative impact on the subsequent coating growth, which is in line with the microstructure as well as the poor corrosion resistance of H₃PO₄/LDH and HCl/LDH samples.

It can be seen from Figs. 16(c₁−c₃), (d₁−d₃) and Fig. 17(c) that the surface area fraction of Al−Mn phase on the surface of HNO₃/AZ31 and CA/AZ31 increases initially and then tends to be constant with the increase of the pretreatment time. In Figs. 16(c₁−c₄), it is noted that with further increase in the pretreatment time, the corrosion becomes
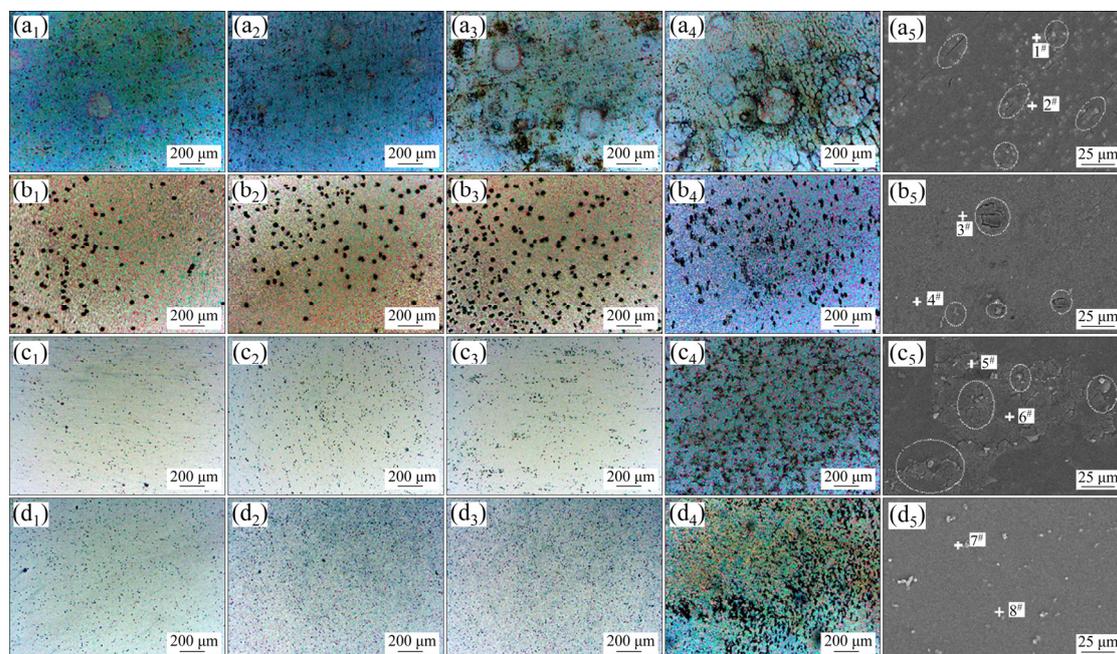

Fig. 16 Optical microstructures ((a₁−a₄): H₃PO₄/AZ31-5 s, 15 s, 30 s and 45 s, respectively; (b₁−b₄): HCl/AZ31-3 s, 5 s, 10 s and 20 s, respectively; (c₁−c₄): HNO₃/AZ31-3 s, 5 s, 10 s and 20 s, respectively; (d₁−d₄): CA/AZ31-5 s, 15 s, 30 s and 45 s, respectively), and FE-SEM images (a₅, b₅, c₅ and d₅) of (a₄, b₄, c₄ and d₄), respectively

Table 7 Elemental compositions of selected spectra shown in Fig. 16 (at.%)

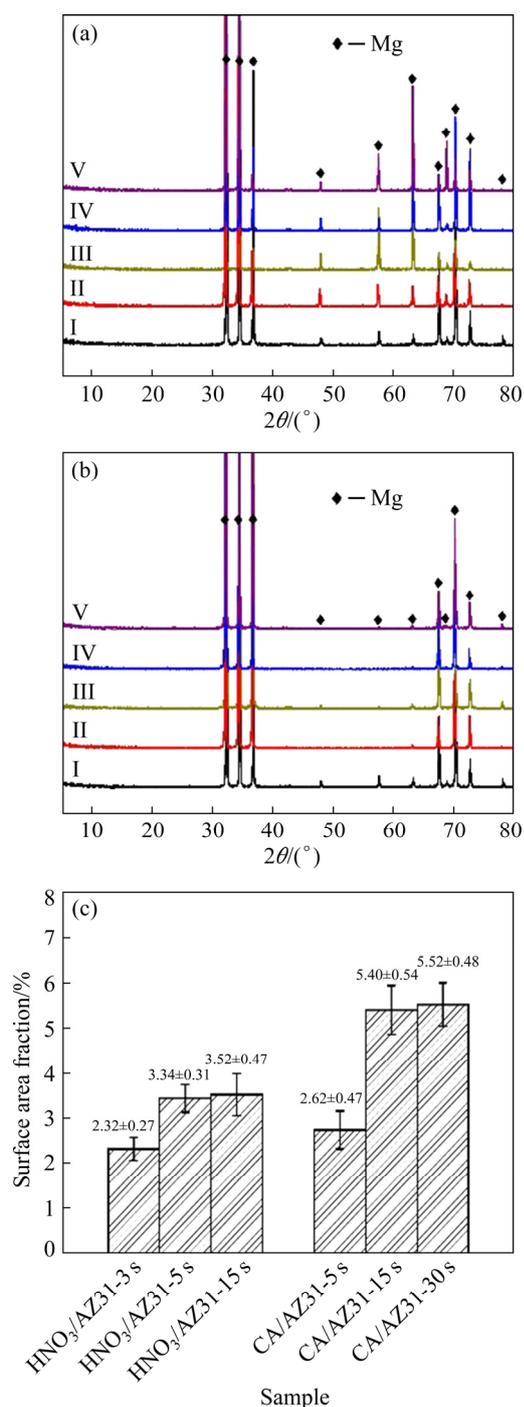| Spectrum No.	Mg	C	O	Al	Mn	Cl	P
1#	2.14			72.23	25.64		
2#	62.93		29.05	2.24			5.78
3#	37.69			45.35	16.96		
4#	23.06	14.43	54.17	0.80		7.55	
5#	7.83			67.28	24.90		
6#	71.48	24.25	2.75	1.14	0.12		
7#	35.60			44.38	20.02		
8#	16.93	73.97	8.64	0.39	0.08		

Fig. 17 (a) XRD patterns of AZ31 Mg alloy (I), H₃PO₄/ AZ31-15 s (II), HCl/AZ31-5 s (III), HNO₃/AZ31-5 s (IV) and CA/AZ31-15 s (V); (b) XRD patterns of AZ31 Mg alloy (I), H₃PO₄/AZ31-45 s (II), HCl/AZ31-20 s (III), HNO₃/AZ31-20 s (IV) and CA/AZ31-45 s (V); (c) Surface area fractions of Al−Mn phase of HNO₃/ AZ31 and CA/AZ31 pretreated for different time

severer. The corrosion in Fig. 16(c₄) is the severest, and the corrosion pits and cracks appear on the surface of HNO₃/AZ31-20 s as highlighted with a white circle in the corresponding Fig. 16(c₅). As for

CA/AZ31-45 s sample, no obvious corrosion cracks and corrosion pits are observed. The reason is that citric acid is relatively mild which has less damage to the substrate during the pretreatment period. It is noticed that the amount of Al−Mn phase on the surface of the AZ31 substrate pretreated with 45 s decreases as compared to that of the sample pretreated with 15 s (Fig. 16(d₂)), which may be due to the coverage of the corrosion products.

Figure 17 exhibits the XRD patterns of the AZ31 substrate pretreated with acid for various periods and the surface area fraction of Al−Mn phase on the surfaces. Interestingly, the characteristic peaks of the corrosion products on H₃PO₄/AZ31-45 s and HCl/AZ31-20 s surfaces are not detected (Fig. 17(b)), which may be due to the low amount of the corrosion products. Besides, it can be found that the XRD diffraction peaks of the acid pretreatment samples here are almost unchanged as compared to the base AZ31 alloy (Fig. 17(a)), which demonstrates that the acid etching does not significantly change the substrate. However, the characteristic peaks of the α-Mg phase of all samples at 2θ values of 47.8°, 57.3° and 63.1° almost disappear owing to the coverage of corrosion products (Fig. 17(b)). Therefore, the selection of a proper type of acid and treatment time is very critical for the increase of the surface area fraction of the Al−Mn phase on the AZ31 Mg alloy surface.

4.2 Influence of Al−Mn phase on coating growth and coating performance

In our previous research [1], it was found that the second phase of the alloy had an important effect on the film formation process. For example, the Al−Mn phase in the AM30 and AZ31 Mg alloys can be used as an initiator to form a calcium-doped zinc phosphate coating [31]. The surface morphology and anti-corrosion performance of the subsequently grown coating will be affected by the size and distribution of Al−Mn particles. Therefore, we speculate that the Al−Mn phase may play an important role in the formation of LDH coating. In order to investigate the effect of CA treatment on the growth process of LDH coating, we adopted 0.5, 1.5 and 3 h as the acid treatment period.

Figure 18 shows the SEM images of polished AZ31 and LDH coatings pretreated by CA under
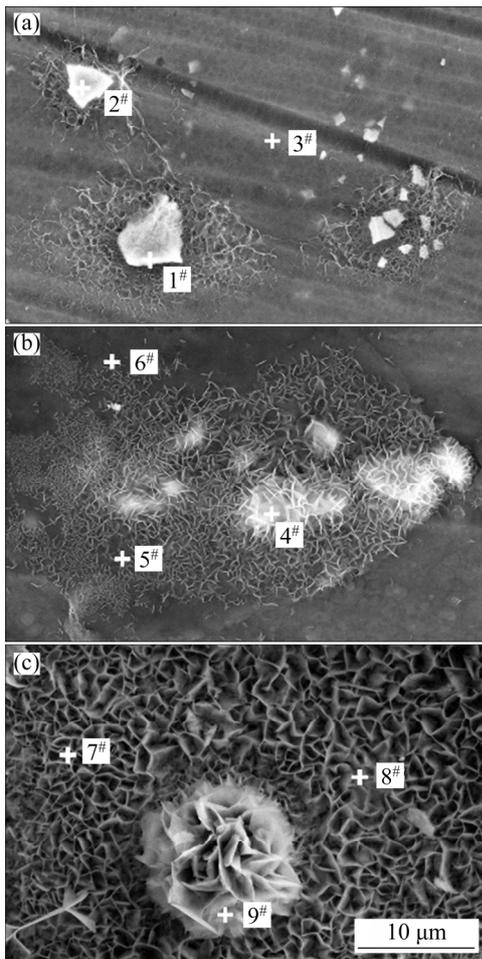
Fig. 18 FE-SEM images of CA/LDH-0.5 h (a), CA/LDH-1.5 h (b) and CA/LDH-3 h (c)

Table 8 Elemental compositions of selected spectra on LDH coating shown in Fig.18 (at.%)

Spectrum No.	Mg	O	Al	C	Mn
1[#]	4.99	12.85	33.75	24.5	23.91
2[#]	43.61	15.20	12.41	21.73	7.05
3[#]	70.13	6.24	1.09	22.53	−
4[#]	15.59	25.08	21.37	28.83	9.13
5[#]	68.40	10.97	2.10	18.54	−
6[#]	68.47	9.99	1.46	20.00	0.08
7[#]	19.47	63.19	1.22	16.13	−
8[#]	23.94	61.34	1.68	13.04	−
9[#]	25.95	62.01	2.37	9.66	−
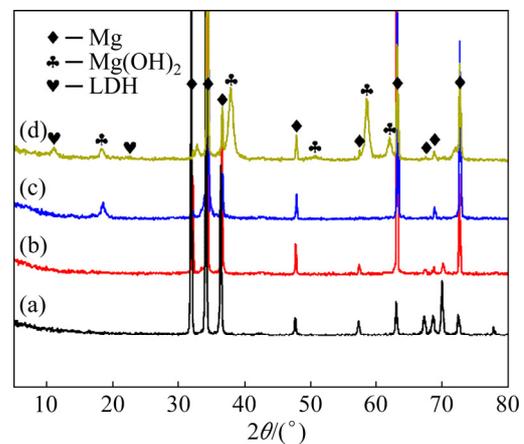
Fig. 19 XRD patterns of AZ31 Mg alloy (a), CA/LDH-0.5 h (b), CA/LDH-1.5 h (c) and CA/LDH-3 h (d)

different reaction time. The corresponding element contents are shown in Table 8 and the XRD patterns are displayed in Fig. 19. It is noteworthy that there are higher contents of Al and Mn at the nucleation site of $Mg(OH)_2$ as seen in Table 8 (Spectra 1[#] and 2[#]), which means that the nucleation is located nearby the Al−Mn phase on the AZ31 substrate (Al_8Mn_5 and AlMn). At the initial stage of the reaction i.e., 0.5 h (Fig. 18(a)), a small amount of $Mg(OH)_2$ precipitates preferentially around the Al−Mn phase. The reason is that the Al−Mn phase with higher potential acts as the cathode, and the lower potential α-Mg acts as the anode for galvanic corrosion. As a result, α-Mg dissolves and immediately combines with OH^- ions around the Al−Mn phase to generate $Mg(OH)_2$. The specific chemical reactions are as follows:
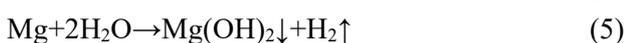
$$Mg \rightarrow Mg^{2+}+2e \qquad (3)$$

$$2H_2O+2e \rightarrow H_2\uparrow+2OH^- \qquad (4)$$

$$Mg+2H_2O \rightarrow Mg(OH)_2\downarrow+H_2\uparrow \qquad (5)$$

As the treatment time increases, the $Mg(OH)_2$ precipitate around the Al−Mn phase gradually grows. It can be seen from Fig. 18(b) that $Mg(OH)_2$ presents a three-dimensional porous network structure. It should be noted that $Mg(OH)_2$ surrounds the Al−Mn phase as the center and suggesting gradual diffusion outward. After 3 h of immersion treatment, the entire AZ31 substrate is completely covered by sheet-like morphology, which is vertically interlaced over the surface of the AZ31 Mg alloy as shown in Fig. 18(c). It can be seen that at the beginning of the reaction, no obvious LDH peaks and $Mg(OH)_2$ peaks appear in Fig. 19(b), but with the prolongation of the reaction time, we observe diffraction peaks of $Mg(OH)_2$, as shown in Fig. 19(c), and after 3 h of reaction, the diffraction peaks of LDH appear. From the XRD pattern shown in Fig. 19(d), we know that the basic ingredients of the coating are LDH and $Mg(OH)_2$. The specific chemical reactions are as

follows [39,40]:

$$CO_2+H_2O \rightarrow CO_3^{2-}+2H^+ \tag{6}$$

$$2Mg(OH)_2+Al^{3+}+3OH^- \rightarrow Mg_2Al(OH)_7 \tag{7}$$

$$3Mg_2Al(OH)_7+OH^-+4.5H_2O \rightarrow \\ Mg_6Al_2(OH)_{18} \cdot 4.5H_2O+Al(OH)_4^- \tag{8}$$

$$Mg_6Al_2(OH)_{18} \cdot 4.5H_2O+CO_3^{2-} \rightarrow \\ Mg_6Al_2CO_3(OH)_{16} \cdot 4H_2O+2OH^-+0.5H_2O \tag{9}$$
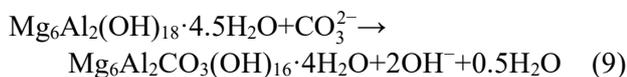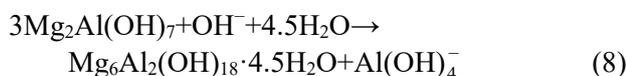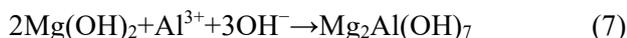
Figure 20 shows the coating thickness and corrosion current density as a function of Al−Mn phase surface area fraction. It is apparent that coating thickness and corrosion current densities of the Samples $1^\#$, $2^\#$ and $3^\#$ are related to the surface area fraction of Al−Mn phase. The higher surface area fraction of Al−Mn phase corresponds to the higher thickness of the coating and the lower corrosion current density. Therefore, we conclude that the Al−Mn phase plays a role in promoting the growth of the coating and thus enhancing the corrosion resistance of the coating.
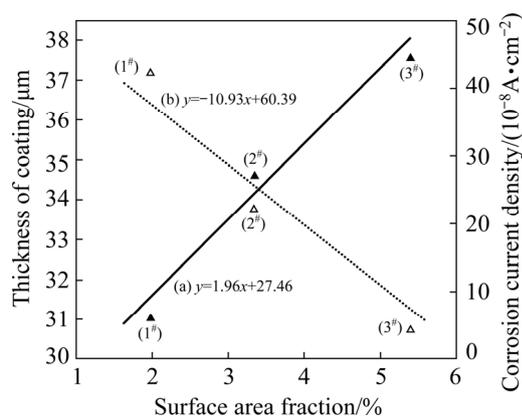

Fig. 20 Relationship between thickness (a) and corrosion current density (b) of LDH ($1^\#$), HNO$_3$/LDH ($2^\#$), CA/LDH ($3^\#$), and surface area fraction of Al−Mn phase

4.3 Influence of CA on coating growth

Figure 21 shows the XPS high resolution spectra of C 1s for CA/AZ31, CA/LDH-0.5 h and CA/LDH-1.5 h. The peaks of C 1s are divided into three peaks: C—C, 284.6 eV; C—O, 286.6 eV; C=O, 288.4 eV and CO_3^{2-}, 289 eV, and the group of C=O corresponds to CA. CA contains carboxyl groups, and carboxyl groups have complexing ability with metal ions [10], which likely facilitate the Mg^{2+} and Al^{3+} reaction during the formation of LDH coating. In order to further explore the role of CA, the C 1s curve fitting for different reaction time is analyzed (Fig. 21). The presence of CA on

the surface of AZ31 substrate after CA pretreatment suggests that CA forms complexes with the free metal ions during the pretreatment process. At this stage, CA complexing with Mg^{2+} is easier to achieve, because at this time the dissolution of α-Mg mainly occurs, and the Mg^{2+} content at the Mg substrate/solution interface is relatively high. After 0.5 h of reaction, the presence of CA can still be detected. Before the formation of LDH, the adsorption of Mg^{2+} and Al^{3+} firstly occurred, and

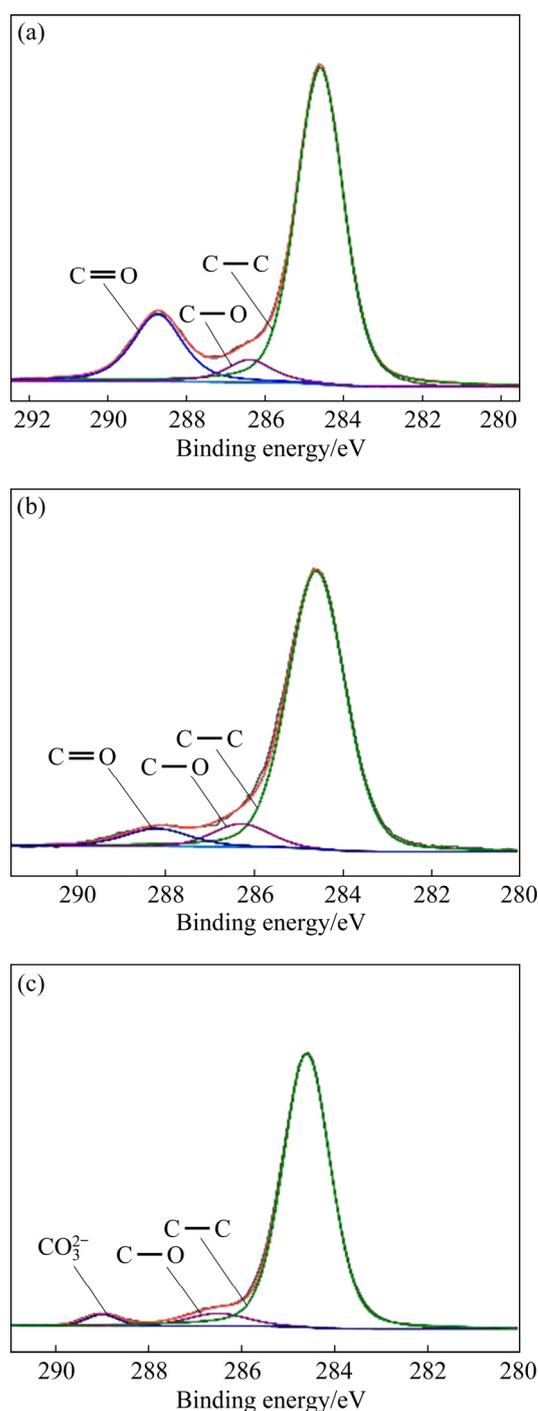**Fig. 21** XPS high resolution spectra of C 1s: (a) CA/AZ31; (b) CA/LDH-0.5 h; (c) CA/LDH-1.5 h

then reacted with OH^- to form $Mg(OH)_2$ and $Al(OH)_3$, suggesting that CA plays an important role in promoting nucleation. However, no CA was detected after 1.5 h of reaction in Fig. 21(c), indicating that CA has no effect in the subsequent growth of LDH coating. Meanwhile, the presence of the CO_3^{2-} group implies that the embedded ion in LDH is CO_3^{2-}. Therefore, it can be inferred that CA plays a crucial role in the initial stage of coating growth.

4.4 Comparison of anti-corrosion performance of polymer coatings on magnesium alloys

In recent years, LDH coatings have been widely used for corrosion protection of AZ31 Mg alloys on account of their unique functionality. The comparison of the corrosion resistance of different LDH coatings is shown in Table 9.

4.5 Coating formation mechanism and corrosion mechanism

Figure 22 shows a schematic diagram of the formation mechanism of steam coating on AZ31

substrate with a prior acid pretreatment. As shown in Fig. 22(a), AZ31 magnesium alloy has α-Mg phase and a second phase (Al−Mn phase). The α-Mg phase is preferentially corroded during acid activation, so the Al−Mn phase as the cathode is basically unaffected (Fig. 22(b)). As a result, the aluminum content of the magnesium alloy surface is increased. In addition, the acid pretreatment activation can also dissolve oxides and hydroxide layer on the surface of magnesium alloy and thus increase the surface roughness [28]. When the magnesium alloy is placed in a Teflon-lined autoclave, the steam generated by the water under high temperature and high pressure has high kinetic energy and reactivity. The steam reacts with the Mg^{2+} and Al^{3+} ions released from the AZ31 Mg alloy firstly, and then $Mg(OH)_2$ and Mg−Al−CO_3^{2-}−LDH are formed (Figs. 22(c) and (d)). Carbonate ions are formed by the reaction of steam and carbon dioxide in the closed autoclave.

Figure 23 shows a schematic diagram of the corrosion mechanism of the steam coating on the AZ31 substrate with a prior acid pretreatment. In

Table 9 Corrosion resistance of LDH coatings on Mg alloys in NaCl solution

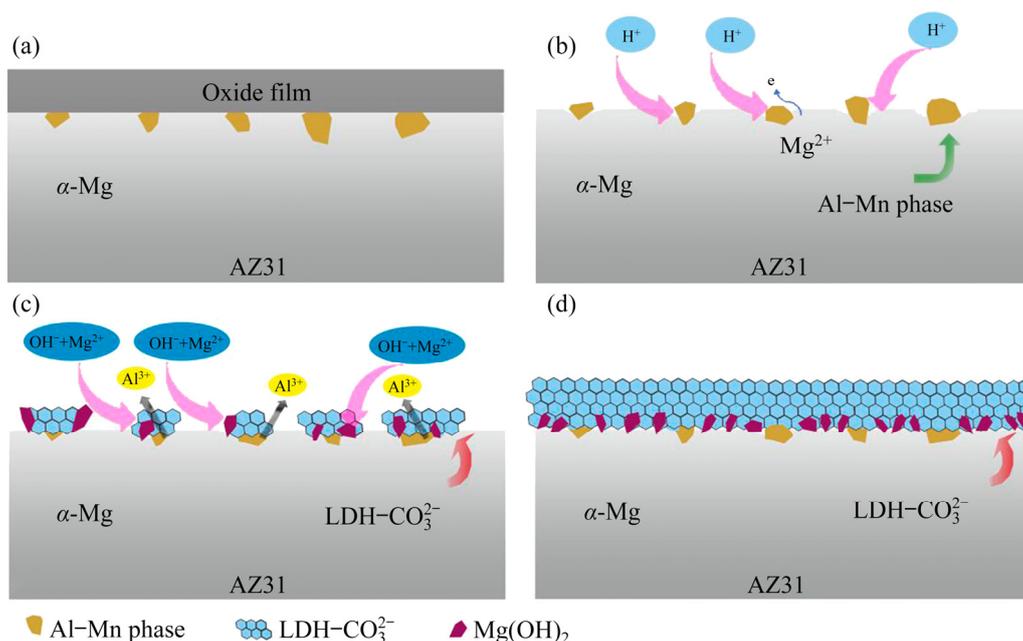| Coating	Substrate	Thickness/ μm	Electrolyte	$J_{corr}/(A \cdot cm^{-2})$		φ_{corr}(vs SCE)/V		Source
				Substrate	Coating	Substrate	Coating	
AO/LDH	AZ31	3.90	3.5 wt.% NaCl solution	1.47×10^{-5}	7.90×10^{-7}	−1.06	−0.33	[41]
CA/LDH	AZ31	37.65	3.5 wt.% NaCl solution	1.42×10^{-5}	4.46×10^{-8}	−1.46	−1.28	Present work

Fig. 22 Schematic diagram of formation mechanism of steam coating on AZ31 substrate with prior acid pretreatment
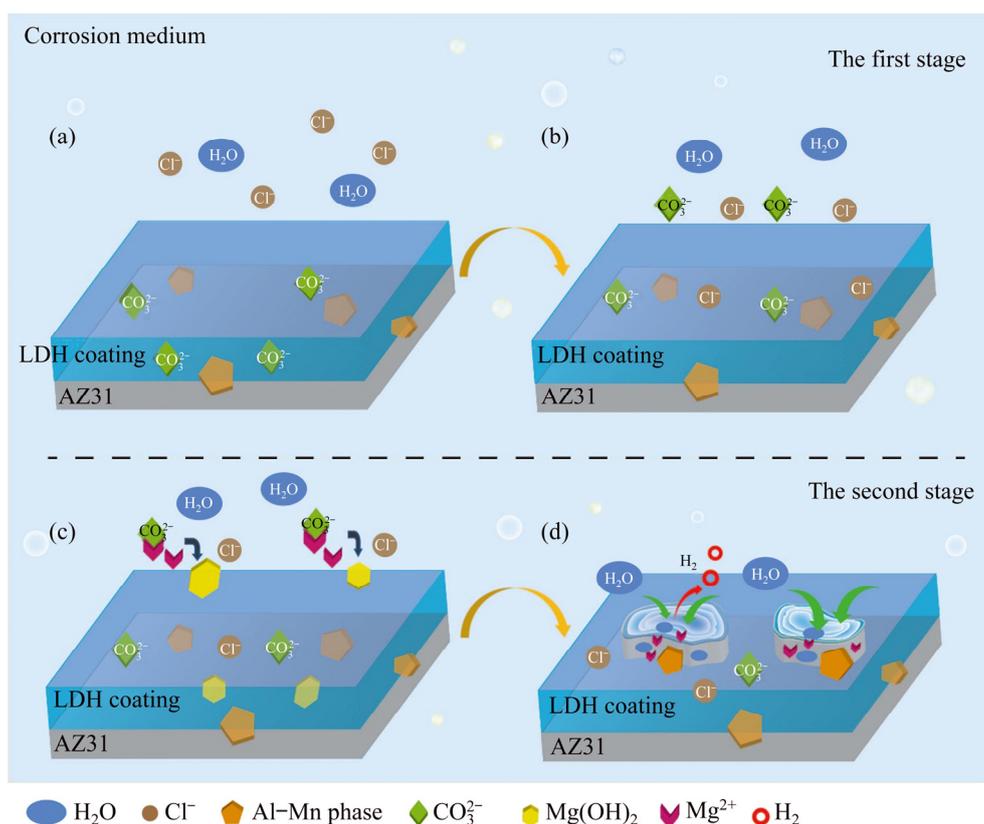
Fig. 23 Schematic diagram of corrosion mechanism of steam coating on AZ31 substrate with prior acid pretreatment

the first stage of corrosion (Figs. 23(a) and (b)), when the sample is immersed in 3.5 wt.% NaCl solution, the Cl^- ions in the solution diffuse into the solution/coating interface, and are trapped by LDH (Fig. 23(b)) This prevents that the soluble chlorides are formed in the coating and can provide the protection effect to the coating. The specific chemical reaction is as follows:

$$LDH-CO_3^{2-}+Cl^-\rightarrow LDH-Cl^-+CO_3^{2-} \qquad (10)$$
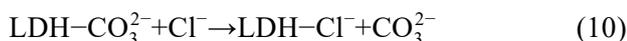
On the other hand, the anions CO_3^{2-} released in the LDH intercalation diffuse to the coating/solution interface and gather on the coating surface to form a diffusion boundary layer (Fig. 23(b)). The concentration of CO_3^{2-} ions at the coating/solution interface is high, and they act as cationic corrosion inhibitors (such as Mg^{2+} ions). The existence of competitive adsorption reduces the diffusion of Cl^- ions of the solution into the solution/coating interface, thereby reducing the damage of Cl^- ions to the coating.

As the immersion time increases, coating damage (for example, pitting) begins to occur at the position where defects exist (for example, near the Al−Mn phase). At this time, the CO_3^{2-} ions in the diffusion boundary layer react with the dissolved

Mg^{2+} ions to form an insoluble precipitate of $MgCO_3$, which is easily converted to the less soluble $Mg(OH)_2$ under alkaline conditions (Fig. 23(c)). The corrosion product $Mg(OH)_2$ covers the pits, thus forming secondary protection. The specific chemical reactions are as follows:

$$Mg^{2+}+CO_3^{2-}\rightarrow MgCO_3\downarrow \qquad (11)$$

$$MgCO_3+2OH^-\rightarrow Mg(OH)_2\downarrow+CO_3^{2-} \qquad (12)$$
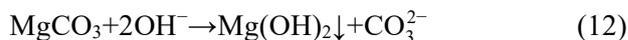
In the second stage of corrosion, H_2O molecules in the solution gradually penetrate into the coating/substrate interface through defects or pores in the coating (usually near the Al−Mn phase), forming micro-galvanic corrosion (Fig. 23(d)). Mg undergoes a dissolution reaction to generate a large amount of $Mg(OH)_2$ and H_2. At the same time, Cl^- ions can replace OH^- ions in $Mg(OH)_2$ to form $MgCl_2$ with higher solubility in water, destroying the corrosion product film of $Mg(OH)_2$. Finally, due to the volume expansion of corrosion products and upward forces exerted by H_2, the LDH coating experiences a large amount of mechanical stress, which causes the coating to crack (Fig. 23(d)). The specific chemical reaction is as follows:

$$Mg(OH)_2+2Cl^-\rightarrow MgCl_2+2OH^- \qquad (13)$$
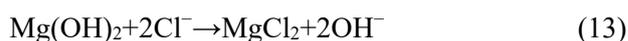
5 Conclusions

(1) A significant amount of Al−Mn phase is exposed on the surface of AZ31 Mg alloy after HNO_3 or CA pretreatment, while no Al−Mn phase appears on the surface of the alloy after H_3PO_4 or HCl pretreatment. The surface area fraction of the Al−Mn phase increases up to about two times for the HNO_3-pretreated alloy and about three times for the CA-pretreated alloy as compared to the polished alloy. H_3PO_4 and HCl have no effect on the quantity of the Al−Mn phase exposed on the surface of the alloy, while CA and HNO_3 have a positive effect on the increment of the exposed Al−Mn phase. The Al−Mn phase plays a significant role in promoting the growth of the LDH coating.

(2) Compared with the LDH coating prepared without acid pretreatment (J_{corr} is $4.22\times10^{-7}A/cm^2$), the process of HNO_3 or CA pretreatment boosts the corrosion resistance of the prepared LDH coating. Among them, the J_{corr} of the CA/LDH coating is $4.46\times10^{-8}A/cm^2$, which is three orders of magnitude lower than that of the bare alloy and one order of magnitude lower than that of the LDH coating on the alloy without pretreatment. The results indicate that CA pretreatment can dramatically boost the anti-corrosion performance of the steam coating on the alloy.

(3) Acid pretreatment of the alloy activates the surface of the alloy via exposing the intermetallic Al−Mn particles. The magnesium matrix (anode) is preferentially corroded while the aluminum-rich Al−Mn phase (cathode) is unaffected, and thereby increases the aluminum content on the surface of the alloy. Interestingly, Al−Mn phase provides more nucleation sites for the LDH coating growth, which promotes the formation of the LDH coating. Therefore, it can be concluded that a suitable acid pretreatment can enhance the corrosion resistance performance of the LDH coating on AZ31 Mg alloy.

Acknowledgments

References

[1] DING Zi-you, CUI Lan-yue, CHEN Xiao-bo, ZENG Rong-chang, GUAN Shao-kang, LI Shuo-qi, ZHANG Fen, ZOU Yu-hong, LIU Qing-yun. In vitro corrosion of micro-arc oxidation coating on Mg−1Li−1Ca alloy—The influence of intermetallic compound Mg_2Ca [J]. Journal of Alloys and Compounds, 2018, 764: 250−260.

[2] GU Dong-dong, WANG Jia-wen, CHEN Yu-bin, PENG Jian. Effect of Mn addition and refining process on Fe reduction of Mg−Mn alloys made from magnesium scrap [J]. Transactions of Nonferrous Metals Society of China, 2020, 30: 2941−2951.

[3] ZHANG Zhao-qi, ZENG Rong-chang, LIN Cun-guo, WANG Li, CHEN Xiao-bo, CHEN Dong-chu. Corrosion resistance of self-cleaning silane/polypropylene composite coatings on magnesium alloy AZ31 [J]. Journal of Materials Science & Technology, 2020, 41: 43−55.

[4] XIA Yu, WU Liang, YAO Wen-hu, HAO Meng, CHEN Jing, ZHANG Cheng, WU Tao, XIE Zhi-hui, SONG Jiang-feng, JIANG Bin, MA Yan-long, PAN Fu-sheng. In-situ layered double hydroxides on Mg−Ca alloy: Role of calcium in magnesium alloy [J]. Transactions of Nonferrous Metals Society of China, 2021, 31: 1612−1627.

[5] ZHOU He, LIU Jin-shui, ZHOU Dian-wu, TAO Tao. Effect of Al-foil addition on microstructure and temperature field of laser fusion welded joints of DP590 dual-phase steel and AZ31B magnesium alloy [J]. Transactions of Nonferrous Metals Society of China, 2020, 30: 2669−2680.

[6] CHEN X B, BIRBILIS N, ABBOTT T B. Effect of Ca^{2+} and PO_4^{3-} levels on the formation of calcium phosphate conversion coatings on die-cast magnesium alloy AZ91D [J]. Corrosion Science, 2012, 55: 226−232.

[7] YIN Zheng-zheng, QI Wei-chen, ZENG Rong-chang, CHEN Xiao-bo, GU Chang-dong, GUAN Shao-kang, ZHENG Yu-feng. Advances in coatings on biodegradable magnesium alloys [J]. Journal of Magnesium and Alloys, 2020, 8: 42−65.

[8] WU Wei, SUN Xiang, ZHU Chun-liu, ZHANG Fen, ZENG Rong-chang, ZOU Yu-hong, LI Shuo-qi. Biocorrosion resistance and biocompatibility of Mg−Al layered double hydroxide/poly-*L*-glutamic acid hybrid coating on magnesium alloy AZ31 [J]. Progress in Organic Coatings, 2020, 147: 105746.

[9] YAO Qing-song, ZHANG Fen, SONG Liang, ZENG Rong-chang, CUI Lan-yue, LI Shuo-qi, WANG Zhen-lin, HAN En-hou. Corrosion resistance of a ceria/polymethyltrimethoxysilane modified Mg−Al-layered double hydroxide on AZ31 magnesium alloy [J]. Journal of Alloys and Compounds, 2018, 764: 913−928.

[10] FAN Xiao-li, LI Chang-yang, WANG Yu-bo, HUO Yuan-fang, LI Shuo-qi, ZENG Rong-chang. Corrosion resistance of an amino acid-bioinspired calcium phosphate coating on magnesium alloy AZ31 [J]. Journal of Materials Science & Technology, 2020, 49: 224−235.

[11] JI Xiao-jing, GAO Ling, LIU Jia-cheng, JIANG Run-zheng, SUN Feng-yu, CUI Lan-yue, LI Shuo-qi, ZHI Ke-qian, ZENG Rong-chang, WANG Zhen-lin. Corrosion resistance

and antibacterial activity of hydroxyapatite coating induced by ciprofloxacin-loaded polymeric multilayers on magnesium alloy [J]. Progress in Organic Coatings, 2019, 135: 465−474.

[12] WANG Zhi-hu, ZHANG Ju-mei, LI Yan, BAI Li-jing, ZHANG Guo-jun. Enhanced corrosion resistance of micro-arc oxidation coated magnesium alloy by superhydrophobic Mg−Al layered double hydroxide coating [J]. Transactions of Nonferrous Metals Society of China, 2019, 29: 2066−2077.

[13] CHEN Jia-ling, FANG Liang, WU Fang, ZENG Xian-guang, HU Jia, ZHANG Shu-fang, JIANG Bin, LUO Hai-jun. Comparison of corrosion resistance of MgAl−LDH and ZnAl−LDH films intercalated with organic anions ASP on AZ31 Mg alloys [J]. Transactions of Nonferrous Metals Society of China, 2020, 30: 2424−2434.

[14] CUI Lan-yue, GAO Ling, ZHANG Jing-chao, TANG Zhe, FAN Xiao-li, LIU Jia-cheng, CHEN Dong-chu, ZENG Rong-chang, LI Shuo-qi, ZHI Ke-qian. In vitro corrosion resistance, antibacterial activity and cytocompatibility of a layer-by-layer assembled DNA coating on magnesium alloy [J]. Journal of Magnesium and Alloys, 2021, 9: 266−280.

[15] WU Liang, YANG Dan-ni, ZHANG Gen, ZHANG Zhi, ZHANG Sheng, TANG Ai-tao, PAN Fu-sheng. Fabrication and characterization of Mg−M layered double hydroxide films on anodized magnesium alloy AZ31 [J]. Applied Surface Science, 2018, 431: 177−186.

[16] ZHANG Gen, WU Liang, TANG Ai-tao, ZHANG Shuo, YUAN Bo, ZHENG Zhi-cheng, PAN Fu-sheng. A novel approach to fabricate protective layered double hydroxide films on the surface of anodized Mg−Al alloy [J]. Advanced Materials Interfaces, 2017, 4: 1700163.

[17] GUO Lian, WU Wei, ZHOU Yong-feng, ZHANG Fen, ZENG Rong-chang, ZENG Jian-ming. Layered double hydroxide coatings on magnesium alloys: A review [J]. Journal of Materials Science & Technology, 2018, 34: 1455−1466.

[18] WANG Qiang, O'HARE D. Recent advances in the synthesis and application of layered double hydroxide (LDH) nanosheets [J]. Chemical Reviews, 2012, 112: 4124−4155.

[19] WU Liang, DING Xing-xing, ZHENG Zhi-cheng, TANG Ai-tao, ZHANG Gen, ATRENS A, PAN Fu-sheng. Doubly-doped Mg−Al−Ce−V$_2$O$_7^{4-}$ LDH composite film on magnesium alloy AZ31 for anticorrosion [J]. Journal of Materials Science & Technology, 2021, 64: 66−72.

[20] WANG Xin, JING Chuan, CHEN Yu-xiang, WANG Xiu-shuang, ZHAO Gang, ZHANG Xing, WU Liang, LIU Xiao-ying, DONG Bi-qin, ZHANG Yu-xin. Active corrosion protection of super-hydrophobic corrosion inhibitor intercalated Mg−Al layered double hydroxide coating on AZ31 magnesium alloy [J]. Journal of Magnesium and Alloys, 2020, 8: 291−300.

[21] CHEN Jun-feng, LIANG Si-yan, FU Dian-bao, FAN Wang-xian, LIN Wen-xin, REN Wei-wei, ZOU Lin-chi, CUI Xi-ping. Design and in situ prepare a novel composite coating on Mg alloy for active anti-corrosion protection [J]. Journal of Alloys and Compounds, 2020, 831: 154580.

[22] SONG Yu-han, TANG Yan, FANG Liang, WU Fang, ZENG Xian-guang, HU Jia, ZHANG Shu-fang, JIANG Bin, LUO Hai-jun. Enhancement of corrosion resistance of AZ31 Mg

alloys by one-step in situ synthesis of ZnAl−LDH films intercalated with organic anions (ASP, La) [J]. Journal of Magnesium and Alloys, 2021, 9: 658−667.

[23] QIU Zai-meng, ZENG Rong-chang, ZHANG Fen, SONG Liang, LI Shuo-qi. Corrosion resistance of Mg−Al LDH/Mg(OH)$_2$/silane−Ce hybrid coating on magnesium alloy AZ31 [J]. Transactions of Nonferrous Metals Society of China, 2020, 30: 2967−2979.

[24] ZHANG Gen, WU Liang, TANG Ai-tao, MA Yan-long, SONG Guang-ling, ZHENG Da-jiang, JIANG Bin, ATRENS A, PAN Fu-sheng. Active corrosion protection by a smart coating based on a MgAl-layered double hydroxide on a cerium-modified plasma electrolytic oxidation coating on Mg alloy AZ31 [J]. Corrosion Science, 2018, 139: 370−382.

[25] CHEN Jun, SONG Ying-wei, SHAN Da-yong, HAN En-hou. Study of the corrosion mechanism of the in situ grown Mg–Al−CO$_3^{2-}$ hydrotalcite film on AZ31 alloy [J]. Corrosion Science, 2012, 65: 268−277.

[26] ZENG Rong-chang, LIU Zhen-guo, ZHANG Fen, LI Shuo-qi, CUI Hong-zhi, HAN En-hou. Corrosion of molybdate intercalated hydrotalcite coating on AZ31 Mg alloy [J]. Journal of Materials Chemistry A, 2014, 2: 13049−13057.

[27] ISHIZAKI T, CHIBA S, WATANABE K, SUZUKI H. Corrosion resistance of Mg−Al layered double hydroxide container-containing magnesium hydroxide films formed directly on magnesium alloy by chemical-free steam coating [J]. Journal of Materials Chemistry A, 2013, 1: 8968−8977.

[28] YANG H Y, CHEN X B, GUO X W, WU G H, DING W J, BIRBILIS N. Coating pretreatment for Mg alloy AZ91D [J]. Applied Surface Science, 2012, 258: 5472−5481.

[29] SHI Hao-bo, YU Mei, LIU Jia-hua, RONG Gang, DU Rong-tao, WANG Jie, LI Song-mei. Effect of alkaline etching on microstructure and anticorrosion performance of anodic film on Al−Mg−Si alloy [J]. Corrosion Science, 2020, 169: 108642.

[30] NGUYEN V P, YOU B S, MOON S. Electrodeposition of copper on AZ91 Mg alloy in cyanide solution [J]. Journal of The Korean Institute of Surface Engineering, 2016, 49: 238−244.

[31] ZENG Rong-chang, ZHANG Fen, LAN Zi-dong, CUI Hong-zhi, HAN En-hou. Corrosion resistance of calcium-modified zinc phosphate conversion coatings on magnesium–aluminium alloys [J]. Corrosion Science, 2014, 88: 452−459.

[32] ZENG Rong-chang, CUI Lan-yue, KE Wei. Biomedical magnesium alloys: Composition, microstructure and corrosion [J]. Acta Metallurgica Sinica, 2018, 54: 1215−1235. (in Chinese)

[33] ZENG Rong-chang, LAN Zi-dong, KONG Ling-hong, HUANG Yuan-ding, CUI Hong-zhi. Characterization of calcium-modified zinc phosphate conversion coatings and their influences on corrosion resistance of AZ31 alloy [J]. Surface & Coatings Technology, 2011, 205: 3347−3355.

[34] QIU Zai-meng, ZHANG Fen, CHU Jun-tong, LI Yu-chao, SONG Liang. Corrosion resistance and hydrophobicity of myristic acid modified Mg−Al LDH/Mg(OH)$_2$ steam coating on magnesium alloy AZ31 [J]. Frontiers of Materials Science, 2020, 14: 96−107.

[35] KE Chong, WU Ya-jie, QIU Yao, DUAN Jun-hao, BIRBILIS N, CHEN Xiao-bo. Influence of surface chemistry on the formation of crystalline hydroxide coatings on Mg alloys in liquid water and steam systems [J]. Corrosion Science, 2016, 113: 145−159.

[36] HOU Li-feng, LI Yu-lin, SUN Jun-li, ZHANG Shao-hua, WEI Huan, WEI Ying-hui. Enhancement corrosion resistance of MgAl layered double hydroxides films by anion-exchange mechanism on magnesium alloys [J]. Applied Surface Science, 2019, 487: 101−108.

[37] NAKAMURA K, SHIMADA Y, MIYASHITA T, SERIZAWA A, ISHIZAKI T. Effect of vapor pressure during the steam coating treatment on structure and corrosion resistance of the Mg(OH)2/Mg−Al LDH composite film formed on Mg alloy AZ61 [J]. Materials, 2018, 11: E1659.

[38] WU Bei, LU Shi-xiang, XU Wen-guo, CHENG Yuan-yuan, CUI Shuo. A robust and repairable superhydrophobic Co5Zn21 alloy surface on a zinc substrate [J]. New Journal of Chemistry, 2018, 42: 5408−5414.

[39] LI Chang-yang, GAO Ling, FAN Xiao-li, ZENG Rong-chang, CHEN Dong-chu, ZHI Ke-qian. In vitro degradation and cytocompatibility of a low temperature in-situ grown self-healing Mg−Al LDH coating on MAO-coated magnesium alloy AZ31 [J]. Bioactive Materials, 2020, 5: 364−376.

[40] CHEN Jun, SONG Ying-wei, SHAN Da-yong, HAN En-hou. Study of the in situ growth mechanism of Mg−Al hydrotalcite conversion film on AZ31 magnesium alloy [J]. Corrosion Science, 2012, 63: 148−158.

[41] ZHANG Gen, WU Liang, TANG Ai-tao, CHEN Xiao-bo, MA Yan-long, LONG Ying, PENG Peng, DING Xing-xing, PAN Hui-ling, PAN Fu-sheng. Growth behavior of MgAl-layered double hydroxide films by conversion of anodic films on magnesium alloy AZ31 and their corrosion protection [J]. Applied Surface Science, 2018, 456: 419−429.

金属间化合物 Al−Mn 颗粒对 AZ31 镁合金原位蒸气 Mg−Al−LDH 涂层的影响

李 峰[1]，孙 翔[1]，宋 亮[1]，M. Bobby KANNAN[2,3]，张 芬[1]，
崔蓝月[1]，邹玉红[4]，李硕琦[1]，刘成宝[1]，曾荣昌[1,5]

1. 山东科技大学 材料科学与工程学院 轻金属腐蚀实验室，青岛 266590；
2. School of Engineering, University of Newcastle, Callaghan, New South Wales 2308, Australia;
3. College of Science and Engineering, James Cook University, Townsville, Queensland 4811, Australia;
4. 山东科技大学 化学与环境工程学院，青岛 266590；
5. 郑州大学 材料科学与工程学院，郑州 450002

摘 要：研究金属间合物 Al−Mn 颗粒对 AZ31 镁合金原位形成的 Mg−Al 水滑石(Mg−Al−CO$_3^{2-}$−LDH)蒸气涂层腐蚀行为的影响。该合金用 H$_3$PO$_4$、HCl、HNO$_3$ 或柠檬酸(CA)进行预处理，然后进行水热处理制备 Mg−Al−LDH 涂层。研究涂层样品的显微组织、组成和耐腐蚀性。结果表明，经 CA 预处理后，合金表面暴露的 Al−Mn 相的表面积分数显著增加，促进 Mg−Al−LDH 蒸气涂层的生长。此外，经 CA 预处理后的合金上 LDH 涂层在所有涂层中表面最致密、涂层厚度最大。与裸合金相比，含有涂层样品的腐蚀电流密度降低 3 个数量级。

关键词：镁合金；酸预处理；水滑石；金属间颗粒；蒸气涂层；耐蚀性

(Edited by Wei-ping CHEN)